

The VLA Frontier Fields Survey: A 6 GHz High-resolution Radio Survey of Abell 2744

ESTEBAN A. OROZCO ^{1,2,*}, ERIC F. JIMÉNEZ-ANDRADE ¹, ERIC J. MURPHY ³, IAN SMAIL ⁴,
EMMANUEL MOMJIAN ⁵, IAN HEYWOOD ⁶, MIGUEL A. VEGA,¹ AND CHRISTA DECOURSEY ⁷

¹*Instituto de Radioastronomía y Astrofísica, Universidad Nacional Autónoma de México, Antigua Carretera a Pátzcuaro # 8701, Ex-Hda. San José de la Huerta, Morelia, Michoacán, México C.P. 58089*

²*Observatorio Astronómico de Quito, Escuela Politécnica Nacional, Interior del Parque La Alameda, 170136, Quito, Ecuador*

³*National Radio Astronomy Observatory, 520 Edgemont Road, Charlottesville, VA 22903, USA*

⁴*Centre for Extragalactic Astronomy, Department of Physics, Durham University, South Road, Durham DH1 3LE, UK*

⁵*National Radio Astronomy Observatory, P.O. Box O, Socorro, NM 87801, USA*

⁶*Astrophysics, Department of Physics, University of Oxford, Keble Road, Oxford, OX1 3RH, UK*

⁷*Steward Observatory, University of Arizona, 933 N. Cherry Ave, Tucson, AZ 85721, USA*

ABSTRACT

We present a 6 GHz radio continuum image of the galaxy cluster Abell 2744 ($z = 0.307$) obtained with the *Karl G. Jansky Very Large Array* (VLA) as part of the VLA Frontier Fields program, whose goal is to explore the radio continuum emission from high-redshift galaxies that are magnified by foreground, massive galaxy clusters. With an rms noise of $\approx 1 \mu\text{Jy beam}^{-1}$, at the phase center, and sub-arcsec angular resolution ($\theta_{1/2} = 0''.82$), this is the deepest and most detailed radio image of Abell 2744 ever obtained. A total of 93 sources are detected with a peak signal-to-noise ratio ≥ 5 , of which 46 have optical/near-infrared (IR) counterparts with available redshift, magnification (μ), and stellar mass (M_*) estimates. The radio sources are distributed over a redshift from 0.15 to 3.55, with a median redshift value of $\bar{z} = 0.93$ and a median stellar mass of $\bar{M}_* = 2.3 \times 10^{10} M_\odot$. A comparison between the radio-based star formation rates (SFRs) and those derived from ultraviolet-to-near IR data reveals that the radio SFRs are, on average, an order of magnitude higher than the ultraviolet-to-near IR SFRs. We look for radio counterparts of the so-called “Little Red Dots (LRDs)” galaxies at $z \approx 6$ in Abell 2744, but find no significant detections. After stacking, we derive a 3σ upper limit to the 6 GHz radio luminosity of LRDs of $4.1 \times 10^{39} \text{ erg s}^{-1}$. Finally, we present a sample of 22 moderately/strongly lensed galaxies ($\mu \gtrsim 2$) in the VLA Frontier Fields survey, which is adequate to zoom into star formation processes of main sequence galaxies at $z \approx 1 - 2$.

Keywords: Radio source catalogs (1356) — Star formation (1569) — Gravitational lensing (670) — Very Large Array (1766) — Abell clusters (9)

1. INTRODUCTION

The *Hubble* Frontier Fields (HFF) program originated as a multi-cycle observing campaign using the *Hubble* (*HST*) and *Spitzer* Space Telescopes targeting six strong-lensing galaxy clusters, and six parallel blank fields (Lotz et al. 2017). The Frontier Fields take advantage of the gravitational lensing effect provided by the massive clusters, allowing us to characterize the emission from galaxies that are intrinsically faint or lie at high redshifts. A key goal of the Frontier Fields project

is to collect a substantial sample of these sources and gain insights into the star-formation processes in the early universe, through measurements of stellar mass, star-formation rates (SFRs), and the structure of high-redshift galaxies.

The six galaxy clusters of the Frontier Fields program have been observed at different wavelengths with multiple ground and space observatories, including observations with *Herschel* Space Telescope (Rawle et al. 2016), Atacama Large Millimeter Array (ALMA; González-López et al. 2017; Laporte et al. 2017), and *Chandra* X-ray observatory (Van Weeren et al. 2016; Rahaman et al. 2021). More recently, Heywood et al. (2021) presented 3 and 6 GHz observations taken with

Email: e.orozco@irya.unam.mx

* Instituto de Radioastronomía y Astrofísica (IRyA)

NRAO’s Jansky Very Large Array (VLA) of three HFF clusters (MACSJ0416.1-2403, MACSJ0717.5+3745, and MACSJ1149.5+2223), as part of the VLA Frontier Field project, with a $\sim 1\mu\text{Jy beam}^{-1}$ sensitivity and a sub-arcsecond resolution ($\sim 2\text{ kpc}$ at $z \approx 3$). Observations at 3 and 6 GHz primarily trace star-forming galaxies (SFGs) at $0 < z \lesssim 4$, which emit in the radio band due to synchrotron radiation from electrons accelerated in supernova remnants and free-free continuum emission from hot, ionized HII regions. The link between radio emission and the star formation rate (SFR) can be established using the empirically derived far-infrared–radio correlation (FIRRC), which enables characterization of star formation in high-redshift SFGs without the effects of dust obscuration. The FIRRC is thought to originate from the star formation process in galaxies, as most massive stars ($\geq 8 M_{\odot}$) radiate mainly at ultraviolet (UV) wavelengths, and a fraction of the UV photons are absorbed and remitted in the infrared (IR) range due to thermal dust emission. After several Myrs, these young massive stars explode as supernovae (SNe), accelerating cosmic rays into the magnetic field of their host galaxy and resulting in diffuse synchrotron emission (Helou et al. 1985; Condon 1992; Murphy et al. 2006, 2008; Murphy 2009; Magnelli et al. 2015). In essence, massive stars provide a common origin for the far infrared and synchrotron emission. With respect to others SFR tracers, such as the UV and $\text{H}\alpha$ luminosities, the radio emission is unaffected by dust extinction and characterize efficiently the emission from dust-obscured star-formation (e.g., Chapman et al. 2004)

In the initial data paper by Heywood et al. (2021), 1966 compact radio components at signal-to-noise ratio ($\text{SNR} > 5$) are reported across three fields at 3 GHz and 6 GHz, of which 169 are reported from the narrower 6 GHz maps; 1262 have spectroscopic redshifts (z_{spec}) and 55 have photometric redshifts (z_{phot}), with a median $\bar{z}_{\text{phot}} = 0.88$ and a median angular size of $0''.27 \pm 0''.25$. They detected a total of 13 moderately lensed ($2.1 < \mu < 6.5$) sources, including a radio source that has a demagnified peak brightness of $0.9\mu\text{Jy beam}^{-1}$, making it a candidate for the faintest extragalactic radio source ever detected (Heywood et al. 2021). Using the 3 and 6 GHz images, Jiménez-Andrade et al. (2021) derived the median 3 GHz radio sizes of $R_{\text{eff}} = 1.3 \pm 0.3\text{ kpc}$ for a sample of 98 star-forming galaxies spanning $0.3 \lesssim z \lesssim 3$, with a median stellar mass of $\log(M_*/M_{\odot}) \approx 10.4$. These measurements were compared with the UV/optical sizes derived from *HST* ACS/WFC3 imaging, while the radio continuum traces the bulk of massive star formation, and the optical emission predominantly traces the stellar disk of galaxies.

Jiménez-Andrade et al. (2021) found that the radio size decreases as the SFR increases, and that the optical size is a factor ≈ 2 -3 larger than the measured in the radio—hinting at centrally enhanced star formation activity in these radio-selected SFGs. To further contribute to the characterization of radio continuum emission from high-redshift galaxies, here we present the 6 GHz image and associated radio source catalog of Abell 2744.

1.1. *Abell 2744*

Abell 2744 (hereafter A 2744; a.k.a. AC118; Olowin 1988) is a massive X-ray galaxy cluster at $z = 0.3072$. Its strong gravitational lensing effect (e.g., Smail et al. 1991) made it one of the six massive clusters selected for the *HST* Frontier Fields project (Lotz et al. 2017). A 2744 is located at RA (J2000) = 00h 14m 20.03s and DEC (J2000) = $-30\text{h } 23\text{m } 17.80\text{s}$, with a virial mass of $7.4 \times 10^{14} M_{\odot}$ (Moretti et al. 2022). A 2744 has been extensively observed at multiple wavelengths (e.g., Moretti et al. 2022; Wang et al. 2023; Fujimoto et al. 2023), because it is visible from both northern and southern observatories. A 2744 is also the third strongest lensing galaxy cluster among the six Frontier Fields, which increases the likelihood of identifying strongly lensed systems at high redshifts.

Several observational programs have targeted A 2744 at multiple radio and millimeter (mm) wavelengths with different angular resolutions and sensitivities. For example, the ALMA Frontier Fields project observed A 2744 at $\sim 250\text{ GHz}$ with a resolution of $\approx 2''.2 \times 2''.1$ and a sensitivity $\approx 55\mu\text{Jy beam}^{-1}$ (González-López et al. 2017). Later, Laporte et al. (2017) use the observations to perform the photometry analysis. More recently, Fujimoto et al. (2023) present ALMA observations at 230 GHz with an angular resolution of $1''.5 \times 1''.5$ and a sensitivity of $32.7\mu\text{Jy beam}^{-1}$.

At radio frequencies, Pearce et al. (2017) with the VLA in the 1–2 GHz L-band and 2–4 GHz S-band receivers in the DnC-, CnB-, and BnA-array configurations achieves a sensitivity of $15\mu\text{Jy beam}^{-1}$ with a resolution of $5''.0 \times 5''.0$. Observations were performed with the Giant Metrewave Radio Telescope (GMRT) array, using 235-MHz and 610-MHz dual bands, achieving a resolution of $3''.5 \times 3''.5$ with a sensitivity of $\approx 100\text{ mJy beam}^{-1}$ (Paul et al. 2019). Our 6 GHz image with an angular resolution of $0''.82 \times 0''.82$ and depth of $\sim 1\mu\text{Jy beam}^{-1}$, is therefore the deepest and sharpest radio/sub-mm image ever obtained in this field.

This paper describes the observations, data reduction, and the production and validation of the 6 GHz radio data products in the A 2744 field. An overview of the

VLA radio observations of A 2744, the imaging methods, and the data reduction process are described in Section 2. The sources extraction method and the radio sizes of our 6 GHz sample are presented in Section 3. The counterpart association is discussed in Section 4. Section 5 presents the properties of our source catalog, including magnification, redshift, and stellar mass distributions. It also describes the methods used for active galactic nuclei (AGN) identification, the derivation and comparison of SFRs based on radio and u -band data, a comparison of the specific star formation rates (sSFRs) with those from other studies focused on magnified galaxies, and the procedure to search for the puzzling population of “Little Red Dots” (LRDs) in our map. The assumed cosmological model throughout this paper is Λ -CDM with $H_0 = 70 \text{ km s}^{-1} \text{ Mpc}^{-1}$, $\Omega_M = 0.3$, and $\Omega_\Lambda = 0.7$.

2. VLA DATA, CALIBRATION AND IMAGING

The data are obtained through the VLA projects 16B-319 (PI: E. Murphy) and 22A-017 (PI: E. Jimenez-Andrade), as part of the VLA Frontier Fields Survey (Heywood et al. 2021). These observational campaigns include observations in the A and C configurations using C-band receivers (4–8 GHz), which provide high spatial resolution while capturing diffuse and extended radio emissions; in this work, we exclusively utilize these datasets. The respective integration time on-source is 3.75 hours for the 22A-017 project, with 3 scheduling blocks in the C configuration; while for the 16B-319 project, the time on-source is 7 hour, with 7 scheduling blocks in the C configuration and 1 scheduling block in the A configuration. Each of the 11 scheduling blocks (SB) is processed with the NRAO CASA pipeline version 2022.2.0.64. The pipeline performs flagging of data affected by antenna shadowing, zero visibility amplitudes, and the initial integrations during the antenna slewing. Additionally, a first pass of radio frequency interference (RFI) excision is applied to both calibrator and target scans. Following the execution of the pipeline, spectral windows (SPWs) with anomalously high amplitudes and/or RFI are identified and flagged.

To produce the 6 GHz continuum image of A 2744, the `tclean` task in CASA was used. The image size is set to 5808 pixels or $871''.2$ to contain a circularized synthesized beam of $\theta_{1/2} = 0''.82$, with a pixel size of $0''.15$. The imaging process is configured with a maximum of 20,000 iterations and a stopping threshold of $3 \mu\text{Jy beam}^{-1}$, corresponding to three times the expected noise level. A Briggs weighting scheme with a robustness parameter of 0.5 is chosen to balance resolution and noise suppression. We adopt the continuum imaging mode (`specmode = mfs`) including a spectral polynomial fit

with two terms (`nterms = 2`) to optimize wide-band imaging. The multi-term, multi-frequency synthesis deconvolver (`deconvolver = mtmfs`) is used, as it is the recommended approach for wide-band, wide-field imaging of sources with varying physical scales. Deconvolution is performed using multiscale cleaning with the wide-field gridding algorithm (`gridder = widefield`) and 64 `w-projection` planes. A primary beam limit of `pblimit = 0.05` is applied to maximize the inclusion of sources without compromising flux reliability.

With this set of parameters, we generate an image with a native resolution of $\theta_{1/2} = 0''.84 \times 0''.23$ at a position angle of 5° , where $\theta_{1/2}$ refers to the full width at half maximum (FWHM) along the major/minor axis of the synthesized beam, respectively. Later, we generate a new version of the map with a circularized synthesized beam of $\theta_{1/2} = 0''.82$ (Figure 1). The pixel brightness distribution of the map, before primary beam correction, is accurately described by a Gaussian function with a standard deviation ($\sigma = 1.09 \mu\text{Jy beam}^{-1}$; see Figure 2). The few deviations from a Gaussian model in the negative end of the histogram are mainly related to the presence of imaging artifacts or spurious sources (see Section 3), while the positive deviations are associated with the radio sources detected in our 6 GHz VLA image.

3. SOURCE EXTRACTION

Since a homogeneous rms noise across images simplifies the source extraction procedure, we adopt the 6 GHz map of A 2744 before primary beam correction to obtain our radio source catalog. To this end, we use the Python Blob Detector and Source Finder (PyBDSF; Mohan & Rafferty 2015) using the default parameters and changing only the `flag_maxsize_fwhm` parameter from 0.3 to 0.2, given that a visual inspection revealed that one extended source (with $\text{FWHM} = 2''.01 \pm 0''.31$) is missed by the default configuration. PyBDSF flags Gaussian sources with contours extending beyond the `flag_maxsize_fwhm` value times the FWHM. Consequently, some sources are omitted. We impose a SNR threshold of 5 to detect peaks of emission, and a SNR threshold of 3 to identify islands of emission, resulting in 117 extracted islands. After a visual inspection, 11 islands are part of 5 different multi-component radio sources, reducing to 106 entries. We only take into account sources located in regions where the primary beam response is larger than 5% ($\approx 6''.26$ away from the phase center), reducing to the 93 radio sources cataloged in this work. The positions, peak brightness, total flux densities, and primary beam corrections from these radio sources are reported in Table 1. We identify five extended radio sources composed

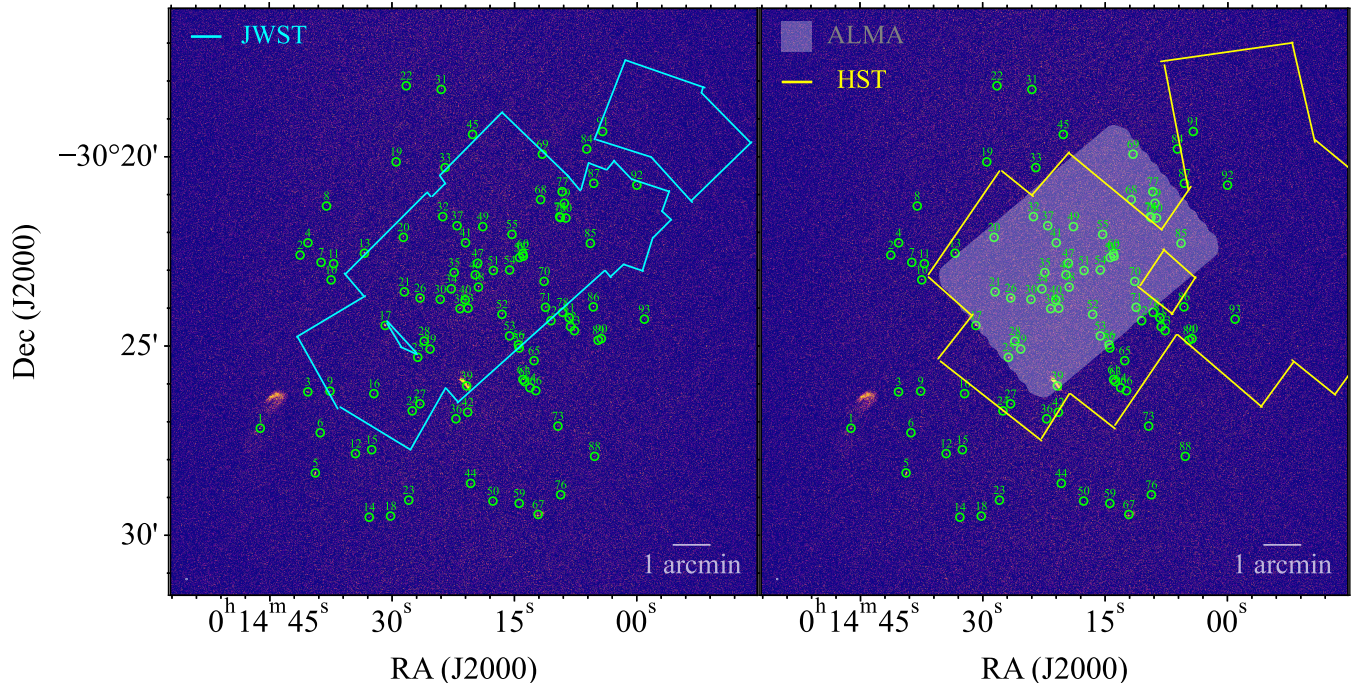


Figure 1. Our 6 GHz image of A 2744. The shaded regions indicate the area covered by the DUALZ Survey uv -tapered image. The cyan contour outlines the *JWST* footprint from the UNCOVER survey, while the yellow contour marks the *HST* footprint from the same survey. Green circles and numbers denote the positions and short IDs (see Table 1) of the radio sources detected in this study.

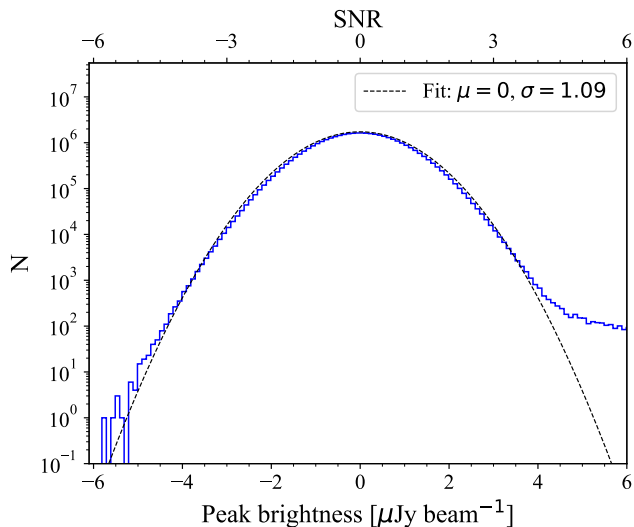


Figure 2. Pixel brightness distribution from the 6 GHz A 2744 map – prior to primary beam correction. The bin width is $0.1 \mu\text{Jy beam}^{-1}$. The dashed line is a Gaussian fit with $\sigma = 1.09 \mu\text{Jy beam}^{-1}$ (i.e., the observed rms noise of the image prior to primary beam correction).

of multiple components (such as FR radio galaxies). To fit their extended emission properly and derive their total flux densities and morphological parameters, we vary

the values of `thresh_is1` and `thresh_pix` parameters in PyBDSF.

To evaluate the reliability of the detected radio sources, we derive the fraction of spurious sources in our catalog. We produce an inverted map by multiplying the 6 GHz continuum map by -1 . Following this, we execute PyBDSF employing the same parameters used to generate the radio source catalog. This process results in the detection of 15 spurious sources with peak $\text{SNR} \leq 8$, leading to a total fraction of spurious sources of 16% and a purity $p > 0.83$ (e.g., González-López et al. 2020; Gómez-Guijarro et al. 2022; Fujimoto et al. 2023), defined as

$$p = \frac{N_{\text{pos}} - N_{\text{neg}}}{N_{\text{pos}}}, \quad (1)$$

where N_{pos} and N_{neg} represent the number of genuine and spurious sources at a given SNR, respectively.

3.1. Radio Size Estimates

PyBDSF provides information on the deconvolved FWHM of the major/minor axis of the radio sources and its uncertainty. Here, we elaborate on how the deconvolved FWHM, i.e., the intrinsic extent of the radio sources, and associated error are derived. In the case of a circular beam, the deconvolved FWHM is given by

$$\theta = \left(\phi^2 - \theta_{1/2}^2 \right)^{1/2}, \quad (2)$$

where ϕ is the FWHM of the fitted major or minor axis of the sources and $\theta_{1/2}$ is the FWHM of the synthesized beam, in our case $\theta_{1/2} = 0''.82$.

The uncertainties in the deconvolved FWHM are computed as in [Murphy et al. \(2017\)](#) using

$$\left(\frac{\sigma_\theta}{\sigma_\phi}\right) = \left[1 - \left(\frac{\theta_{1/2}}{\phi}\right)^2\right]^{-1/2}, \quad (3)$$

where σ_ϕ is the uncertainty of the FWHM before deconvolution. When the fitted FWHM is equal or smaller than the synthesized beam the deconvolved FWHM values are reported as 0 in [Table 1](#). The associated uncertainties in these cases represent the errors related to the fitted FWHM.

To consider a source as confidently resolved along the major axis, we follow the criterion $\phi_M - \theta_{1/2} < 2\sigma_{\phi_M}$ as in [Murphy et al. \(2017\)](#); [Heywood et al. \(2021\)](#), where ϕ_M and σ_{ϕ_M} are the major axis FWHM of the source before deconvolution and its associated error (provided by PyBDSF). In [Table 1](#), the resolved sources get 0, and unresolved sources get 1. Around 39% of the radio sources in our sample are reliably resolved, i.e., 36 out of the 93 sources in the catalog. Consequently, our data set is mainly composed of upper limits to the galaxy sizes that remain unresolved in our 6 GHz map. To estimate the median properties, we employ survival analysis using the Kaplan–Meier (KM; [Kaplan & Meier 1958](#)) estimator as implemented in the Python package ([lifelines](#); [Davidson-Pilon 2019](#)). This approach incorporates the censored observations (i.e., the upper limits) to reconstruct the true underlying distribution in a maximum-likelihood-style framework ([Feigelson & Nelson 1985](#)).

3.2. Selection Function

To infer the selection function imposed by the radio map properties and our source extraction, we derive the maximum detectable angular size as a function of total flux density, which can be used to estimate the maximum radio source size that can be detected at a given redshift, stellar mass, and SFR. This is done by adopting the relation (see [Appendix C of Murphy et al. 2017](#))

$$\frac{S_{\text{peak}}}{S_{\text{int}}} = 2z^2[1 - \sqrt{\pi}z \exp(z^2)\text{erfc}(z)], \quad (4)$$

where $z \approx 0.50398(\theta_{1/2}/R_{\text{eff}})$, with $\theta_{1/2}$ the FWHM of circular beam and R_{eff} is the effective radius of the radio source. Since the sources reported in this work are marginally resolved, i.e., $R_{\text{eff}} \lesssim \theta_{1/2}$, their effective radii of the radio sizes can be approximated as $R_{\text{eff}} \approx \theta_M/2.430$ ([Murphy et al. 2017](#)), where θ_M is the

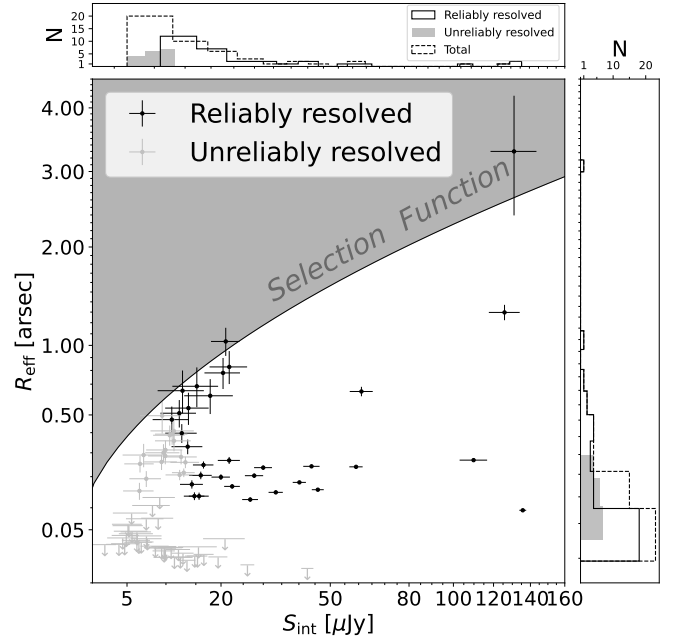


Figure 3. Maximum detectable angular size as a function of the integrated/total flux density of sources in the 6 GHz image of A 2744. Reliably resolved sources are shown in black circles, whereas unreliably resolved sources are presented in gray. In the top panel, counts of reliably/unreliably resolved and total sources are shown as a function of S_{int} . On the right, counts of reliably/unreliably resolved and total sources are shown with respect to the detectable angular size. The vertical arrows are upper limits to the 6 GHz effective radius of sources that are not reliably resolved.

deconvolved FWHM provided by PyBDSF. Then, considering that $S_{\text{peak}} = 5 \mu\text{Jy}$ i.e., our detection threshold, Equation 4 is solved for R_{eff} using the Newton-Raphson method with the `scipy.optimize` library in Python.

The selection function (see [Figure 3](#)) imposed by the resolution and sensitivity of our 6 GHz image of A 2744 shows that we probe sources as faint as $\sim 6.5 \mu\text{Jy}$ with a minimum and maximum FWHM of $\sim 0''.1$ and $\sim 3''.5$ respectively. Close to the detection limit we tend to detect compact sources that, due to their faint nature, are unreliably resolved. On the contrary, the reliably resolved sources are extended and have higher flux densities. The VLA 6 GHz sample has a median effective radius $0''.267$ and 25th/75th percentiles of $0''.198/0''.495$. Our sample also has a median flux density of $15.6 \mu\text{Jy beam}^{-1}$ and 25th/75th percentiles of $11.2/33.4 \mu\text{Jy beam}^{-1}$ (see histograms in [Figure 3](#)). Considering the radio sources with redshift values (see [Section 4](#)), we derive the physical size from the angular sizes extracted by PyBDSF —those values are reported in [Table 1](#).

4. COUNTERPART ASSOCIATION

4.1. *JWST + HST Counterparts*

We cross-match our VLA 6 GHz catalogue with the “UNCOVER Photometric Catalog” presented in Weaver et al. (2024), which includes all the available *JWST*/NIRCam imaging and *HST* ACS/WFC3 deep observations of A 2744. The *JWST* observations are composed of: The Ultra deep NIRSpec and NIRCam observations before the Epoch of Reionization (UNCOVER) Treasure Survey (*JWST*-GO-2561; Bezanson et al. 2024), the Early Release Science (ERS) GLASS-*JWST* program (*JWST*-DD-ERS-1324; Treu et al. 2022), and a Directors(DD) program (*JWST*-DD-276; PI: Chen). The UNCOVER provides deep NIRCam imaging with 4 to 6-hour exposures in the F115W, F150W, F200W, F277W, F356W, F410M, and F444W filters. The GLASS-ERS program provides ultra-deep NIRCam imaging with 9 to 14-hour exposures in the F090W, F115W, F150W, F200W, F277W, F356M, and F444W filters. Finally, the DDT program includes two epochs of NIRCam imaging with an exposure of 1-hour per filter, in the F115W, F150W, F200W, F277W, F356M, and F444W filters. Despite having observations in these multiple bands, the photometric analysis is built from the F277W, F356W and F444W *JWST* filters.

The *HST* observations include *HST*-GO-11689 (PI: Dupke) and *HST*-GO 13386 (PI: Rodney) that perform deep *HST*/ACS imaging in the F435W, F606W, and F814W filters, the *HST*-DD-1395 (PI: Lotz; Lotz et al. 2017) with deep *HST*/WFC3 observations in the F105W, F125W, and F140W filters, the BUF-FALO survey program *HST*-GO-15177 (PIs: Steinhardt & Jauzac; Steinhardt et al. 2020), with ACS and WFC3 observations in the F606W, F814W, F105W, F125W, and F160W filters and most recently the program *JWST*-DD-17231 (PI: Treu). In total, the “UNCOVER Survey” employs 8 *JWST* filters and 7 *HST* filters extending the sky coverage around A 2744, allowing the inclusion of nearby cluster sub-structures.

Using a search radius of $1''.0$, resembling the angular resolution of the 6 GHz image, within the area where the VLA footprint overlaps with the *JWST* coverage, only 48 VLA radio sources are present, and among these, 47 (approximately 98%) have candidate counterparts identified in the *JWST* mosaics. In the case of multiple sources within the search radius (13 cases), the nearest source is adopted as the counterpart. A visual inspection of the 47 radio sources is performed to ensure accurate counterpart associations, which allowed us to discard the apparent *JWST*/*HST* counterpart of the source VLAHFF-J001415.59-302259.85. A detailed visual in-

spection shows that the center of the VLA radio emission does not align with the center of the emission seen in the *JWST + HST* observations (see Figure 13). This clear spatial mismatch indicates that the radio source is unlikely to be physically associated with the galaxy observed by *JWST*, and therefore, the association between these two sources has been discarded. The source, located at ~ 1.44 from the center, has an integrated flux density of $6.92 \mu\text{Jy}$ corresponding to a $\text{SNR} \sim 6.3$. The low significance of the detection suggests that this might be a spurious source (see Section 3).

The counterpart association process yield values for redshift (z), magnification (μ), stellar mass (M_*), and SFR for the 46 VLA radio sources with a *JWST*/*HST* counterpart, see Table 2. Those values are derived by Wang et al. (2023) via spectral energy distribution (SED) fitting using the *Prospector* Bayesian inference framework (Johnson et al. 2021), with two notable modifications. First, observationally-motivated priors on stellar mass, metallicity, and star formation history (SFH) from *Prospector- β* were optimized to improve photometric redshift accuracy (Wang et al. 2023). Second, the magnification–redshift relationship is solved within *Prospector* using mass-dependent priors. The fits were performed using the simple stellar populations (SSPs), come from FSPS (Conroy & Gunn 2010), with MIST isochrones (Choi et al. 2016; Dotter 2016) and MILES stellar library (Bean et al. 2022). The composite stellar populations (CSPs) are modeled with *Prospector- β* (Wang et al. 2023) and dust emission is included in all fits (Draine & Li 2007). The attenuation of the intergalactic medium (IGM) is assumed to follow Madau (1995). The corresponding z , μ , M_* , and SFR distributions are presented in Figure 4 and further discussed in Section 5.1.

4.2. *ALMA Counterparts*

To complement the multi-frequency view of the 46 radio sources that have available *HST + JWST + VLA* information, we look for counterparts in the recently obtained “DUALZ-Deep INCOVER-ALMA Legacy High-Z Survey” (Fujimoto et al. 2023). The DUALZ survey features a contiguous $4' \times 6'$ wide mosaic at 1.2 mm, with a sensitivity of $\sigma = 32.7 \mu\text{Jy beam}^{-1}$. The DUALZ team generated four maps of A 2744; two of them cover a $4' \times 6'$ area and are called “Wide” maps, while the remaining two cover a $2' \times 2'$ area and are called “Deep” maps. In this work, we use one of the “Wide” maps with a synthesized beam size of $1''.81 \times 1''.60$, and a uv -taper of $1''.5 \times 1''.5$, since it covers a more extended area and according to Fujimoto et al. (2023) the uv -taper avoids

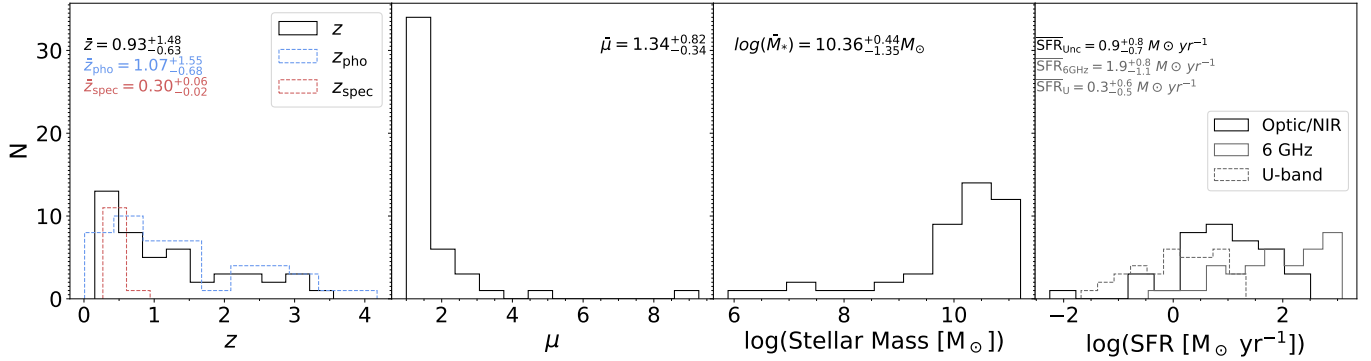


Figure 4. Histograms of redshift (z), magnification (μ), stellar mass (M_*), and SFR values reported by the UNCOVER survey (Weaver et al. 2024) for the 46 VLA radio sources with a *JWST/HST* counterpart. The upper and lower values are the corresponding 16th and 84th percentiles. In the first panel, the black solid line corresponds to the redshift distribution considering z_{phot} and z_{spec} . The blue dashed line corresponds to the photometric redshift distribution and the red dashed line corresponds to the spectroscopic redshift distribution. In the SFR histogram, the optical/NIR SFRs distribution reported by Wang et al. (2023) are shown in a black solid line, while the distribution of the radio-based SFRs derived in this work is shown as a grey solid line, while, the u -band SFRs is given by the dashed gray line. AGN candidates are excluded from the histogram of SFR estimates (see Section 5.2).

missing any strong lensed objects. The footprint of the DUALZ survey is shown in Figure 1.

The DUALZ survey identified 69 sources at $\text{SNR} > 5$ and reports their position, SNR, and 1.2 mm ALMA flux densities with respective errors. We cross-matched the 46 VLA sources with *HST + JWST* counterpart with the ALMA data using a cross-matching radius of $1''0$, in the case of multiple sources in the search radius, the nearest source has been adopted as the counterpart. The result is 20 VLA radio sources with counterparts in the ALMA 1.2 mm map. The corresponding flux densities and ALMA 1.2 mm IDs are reported in Table 2.

In summary, from the 93 VLA 6 GHz-detected sources, 46 sources have an *HST + JWST* counterpart, of which 20 have a counterpart in the ALMA 1.2 mm maps (see flowchart in Figure 5). We produced RGB images for the 46 radio sources with *JWST + HST* counterpart, using the *JWST* NIRCcam filters R: F444W, G: F277W, B: F150W, and overlaid contours of VLA/ALMA emission; see the captions in Figures 12 & 13 for more information. The remaining 47 VLA radio sources without counterparts generally lie outside the *HST*, *JWST*, or/and ALMA mosaics. We note that the VLAHFF-J001404.22-301920.31 falls inside the *HST* and *JWST* mosaics (see Figure 13) but is not detected and/or cataloged by the UNCOVER team. The source is located at $\sim 5''.76$ from the center and reports a flux of $\sim 5.107 \mu\text{Jy}$ corresponding to a $\text{SNR} \sim 5$. According to the analysis presented in Section 3, the low significance of the detection suggests that this is a spurious source.

5. RESULTS

5.1. Magnification, Redshift, Stellar Mass, and Size of Galaxies

The median magnification factor of the 46 sources with *JWST + HST* counterparts in our sample is $\mu = 1.34^{+0.82}_{-0.34}$, based on the 16th, 50th, and 84th percentiles. Only a small fraction ($\approx 24\%$) is moderately lensed, with magnification factors greater than 2 (Figure 6). The source with a highest magnification factor ($\mu = 9.88$) in our sample, VLAHFF-J001413.92-302237.95, has a peak brightness of $8.4 \pm 1.2 \mu\text{Jy beam}^{-1}$ and is located at $z_{\text{phot}} \approx 2.94^{+0.05}_{-0.04}$. The radio-based SFR of this source is $180^{+50}_{-40} \text{M}_{\odot}\text{yr}^{-1}$ with a stellar mass of $\approx 5.5^{+1.2}_{-1.0} \times 10^9 \text{M}_{\odot}$, corresponding to a starburst galaxy that lies above the main sequence of SFGs. The redshift distribution (Figure 6) of the 46 VLA sources with available z values has a median of $\bar{z} = 0.93$ and 16th/84th percentiles of 0.63/1.48, respectively. From the 46 VLA sources with z values reported, 26% (12) of them have spectroscopic redshifts. The source with the highest redshift is VLAHFF-J001419.51-302248.98 ($z_{\text{phot}} \approx 3.55$) with a peak brightness $6.62 \pm 2.45 \mu\text{Jy beam}^{-1}$ and a SFR $\approx 304^{+144}_{-96} \text{M}_{\odot}\text{yr}^{-1}$. The median of the spectroscopic redshift is 0.30 and the 16th/84th percentiles are 0.02/0.06. The distribution of the stellar mass of our sample (Figure 6) has a median of $\log(M_*/\text{M}_{\odot}) = 10.36$ with 16th/18th percentile of (1.33/0.46). The scarcely sampled mass regime below $\log(M_*/\text{M}_{\odot}) \lesssim 9.5$ at higher redshifts ($z \gtrsim 1$) is a result of our radio detection limit that preferentially selects massive, bright systems.

We derived a median 6 GHz size of $R_{\text{eff}} = 1.5^{+1.8}_{-0.4} \text{kpc}$ for the 46 galaxies with reported z_{phot} or z_{spec} in

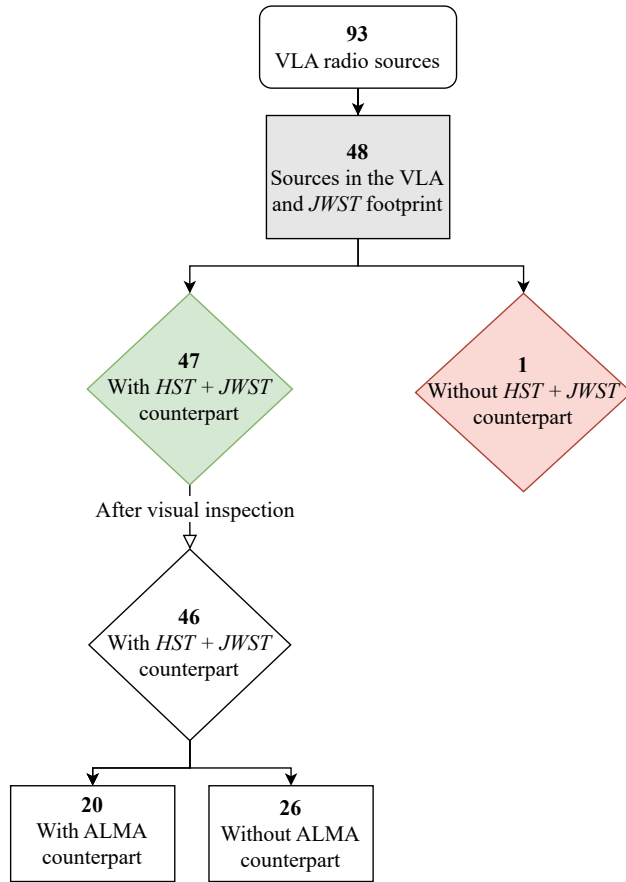


Figure 5. A flowchart that illustrates our matching procedure to identify VLA radio sources with and without counterparts in *JWST*, *HST*, and ALMA imaging. The green color is related to the VLA sources with counterparts and the red color is related to the VLA sources without counterpart.

our sample, were the upper and lower limits are the 95% confidence interval for the media. The sizes of the galaxies at 6 GHz in the three *Hubble* Frontier Fields (MACS J0416.1-2403, MACS J0717.5+3745, and MACS J1149.5+2223) have been previously explored by Jiménez-Andrade et al. (2021). They report a median effective radius of $R_{\text{eff}} = 1.1^{+0.7}_{-0.3}$ kpc for the 31 radio-detected galaxies with $\log(M_*/M_\odot) \approx 10.4$ distributed over $0.3 \lesssim z \lesssim 3$. Our values are consistent with those reported by Jiménez-Andrade et al. (2021), which is expected given that our sample is very similar in terms of redshift and stellar masses, and that we used comparable resolution and sensitivity.

5.2. Identifying AGN Candidates

We have to consider that AGN might be present in our 6 GHz radio source catalog of A2744. Based on the numerical simulations and models of Mancuso et al. (2017) and Bonaldi et al. (2019), the AGN fraction in radio surveys at ≈ 6 GHz detecting sources with total flux densities $\gtrsim 5 \mu\text{Jy}$ is $\approx 14\%$. Thus, our radio source catalog is expected to be dominated by SFGs.

To confirm such predictions and identify AGNs candidates in our 6 GHz radio source catalog of A2744, we first review the work of Labbe et al. (2024) who used the UNCOVER survey data to perform a color-color and morphology selection to identify AGN across $3 < z_{\text{phot}} < 7$. Of the 26 AGN candidates found by Labbe et al. (2024), none match our VLA sources, since our sample is mainly composed by sources at $z < 3$.

We then implement two diagnostics to identify AGN candidates. A source in the 6 GHz catalog is deemed as an AGN candidate if it has an X-ray luminosity $L_X > 10^{42} \text{ erg s}^{-1}$; and/or exhibits an excess of radio emission as expected from the IR-radio correlation of SFGs. To this end, we are limited to the 46 VLA radio sources with z_{spec} and/or z_{phot} reported in UNCOVER.

We use the “The Chandra Source Catalog (CSC)” survey (Evans & Civano 2018) to find X-ray fluxes in the broadband ([0.5-0.7] keV) of our VLA radio sources. Using a cross-match radius of $1''.0$ we find 8 X-ray counterparts, of which 7 meet the first criterion ($L_X > 10^{42} \text{ erg s}^{-1}$) and are deemed as AGN candidates (see Figure 7).

For the second criterion, we search for IR counterparts using the *HST* Frontier Fields *Herschel* catalog presented by Rawle et al. (2016). A search radius of $3''.0$ led to the identification of 6 IR counterparts whose total IR luminosity (L_{IR}), integrated over the rest-frame wavelength range $\lambda = 8 - 100 \mu\text{m}$, spans in a range of $9.3 \lesssim \log(L_{\text{IR}}/L_\odot) \lesssim 12.6$ and are reported by Rawle et al. (2016). We can then infer the expected radio luminosity from the infrared-radio correlation parameterized as Helou et al. (1985)

$$q_{\text{IR}} = \log\left(\frac{L_{\text{IR}}}{3.75 \times 10^{12} \text{ Hz}}\right) - \log\left(\frac{L_{1.4 \text{ GHz}}}{\text{WHz}^{-1}}\right), \quad (5)$$

where L_{IR} is the integrated IR luminosity over the rest-frame wavelength range $\lambda = 8 - 100 \mu\text{m}$ reported by Rawle et al. (2016). While, $L_{1.4 \text{ GHz}}$ is the 1.4 GHz monochromatic radio luminosity.

To identify the radio-excess sources, we use the IRRM models for star-forming galaxies reported by Delhaize et al. (2017),

$$q_{\text{IR}}(z) = (2.88 \pm 0.03)(1+z)^{-0.19 \pm 0.01} \quad (6)$$

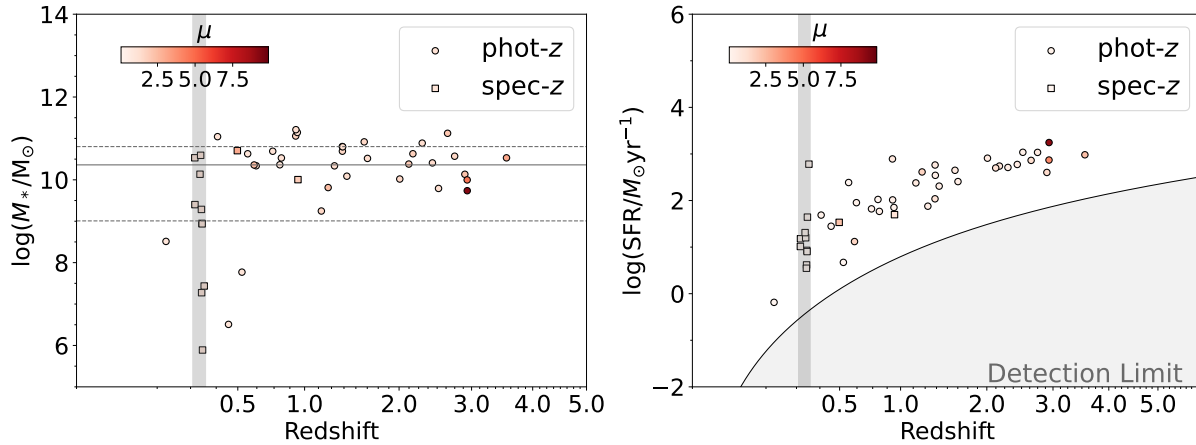


Figure 6. Right panel: Stellar mass as a function of the redshift of the 46 VLA galaxies with *HST+JWST* counterparts, of which 12 have available spectroscopic redshifts (squares). For the remaining 34 galaxies we use photometric redshift (circles). The solid and dashed lines correspond to the 50th, 84th, and 16th percentiles of the stellar mass distribution. Left panel: The SFR of galaxies as a function of redshift. The grey shaded region shows our detection limit without magnification, which is given by the SFR of a galaxy detected at the 5σ level ($\sim 5.45 \mu\text{Jy beam}^{-1}$). The symbols are colored according to the source magnification. The vertical shaded region shows the cluster members. These plots illustrate the advantage of using gravitational lensing to detect less massive/active galaxies at higher redshifts ($z \gtrsim 1$) that could not have been detected without magnification factors larger than 1.

and

$$q_{\text{IR}}(z) = (2.35 \pm 0.08)(1+z)^{-0.12 \pm 0.04} \quad (7)$$

reported by Magnelli et al. (2015). We opt to use these two independent models as a way to improve the robustness of the AGN selection procedure. Figure 7 shows the q_{IR} parameter versus redshift for the 6 VLA sources with IR counterparts along the IRRC models for star-forming galaxies from Magnelli et al. (2015) and Delhaize et al. (2017) with their corresponding 3σ error bounds. Following the results from Radcliffe et al. (2021), the VLA sources with q_{IR} below the mentioned 3σ error bounds are classified as radio excess sources (i.e., AGN candidates). From this criterion 2 AGN candidates were found, one of them (VLAHFF-J001426.56-302344.21) also shows an X-ray luminosity excess fulfilling the first criterion.

Additionally, after a visual inspection it is evident that the VLAHFF-J001446.17-302710.35 source is a radio galaxy with a bright radio lobe, i.e., an AGN. In total, we found 9 AGN candidates. Considering only the VLA sources with z_{spec} and/or z_{phot} reported, the fraction obtained is (9/46; i.e., $\sim 20\%$), which is comparable with the predicted AGN fraction of 14% in μJy -level radio surveys at intermediate frequencies ($\approx 6\text{ GHz}$; Mancuso et al. 2017; Bonaldi et al. 2019).

5.3. Deriving Unobscured and Obscured SFRs

After removing the AGN candidates from our sample, we derive the SFR from the 6 GHz radio emission that is tracing dust-obscured star formation. We use the

SFR calibrations from Murphy et al. (2017), which were normalized to a Chabrier initial mass function (IMF; as used by the UNCOVER team),

$$\left(\frac{\text{SFR}_{6\text{ GHz}}}{M_{\odot}\text{yr}^{-1}}\right) = 4.87 \times 10^{-29} \left(\frac{L_{1.4\text{ GHz}}}{\text{erg s}^{-1}\text{Hz}^{-1}}\right). \quad (8)$$

$L_{1.4\text{ GHz}}$ is given by

$$L_{1.4\text{ GHz}} = \frac{4\pi D_L(z)^2}{(1+z)^{1-\alpha}} \left(\frac{1.4}{6}\right)^{-\alpha} S_{6\text{ GHz}}, \quad (9)$$

where $S_{6\text{ GHz}}$ is the 6 GHz flux density in $\text{erg s}^{-1} \text{cm}^{-2} \text{Hz}^{-1}$, D_L is the luminosity distance in cm, and α is the spectral index. The typical spectral index of radio SFGs is $\alpha \approx 0.7$ with a typical dispersion of ~ 0.10 (e.g., Condon 1992; Smolčić et al. 2017; Klein et al. 2018), introducing further uncertainties to our $\text{SFR}_{6\text{ GHz}}$ estimates.

Typically, SFRs that are not obscured by dust are estimated using observations in $\text{H}\alpha$ and UV, as these tracers are sensitive to the light emitted by young, massive stars. However, for our sources, we lack direct measurements in $\text{H}\alpha$ or UV. Instead, we rely on the Hopkins et al. (2003) calibration, which is derived from $\text{H}\alpha$ observations. This calibration allows us to estimate the unobscured SFR using u -band flux densities from *HST* observations, as reported by the UNCOVER team in their catalogs (Labbe et al. 2024). This approach provides a valuable alternative to assess the star formation activity in our sources despite the absence of direct $\text{H}\alpha$ and UV data.

The unobscured SFR of galaxies is estimated using the rest-frame u -band flux densities reported from the

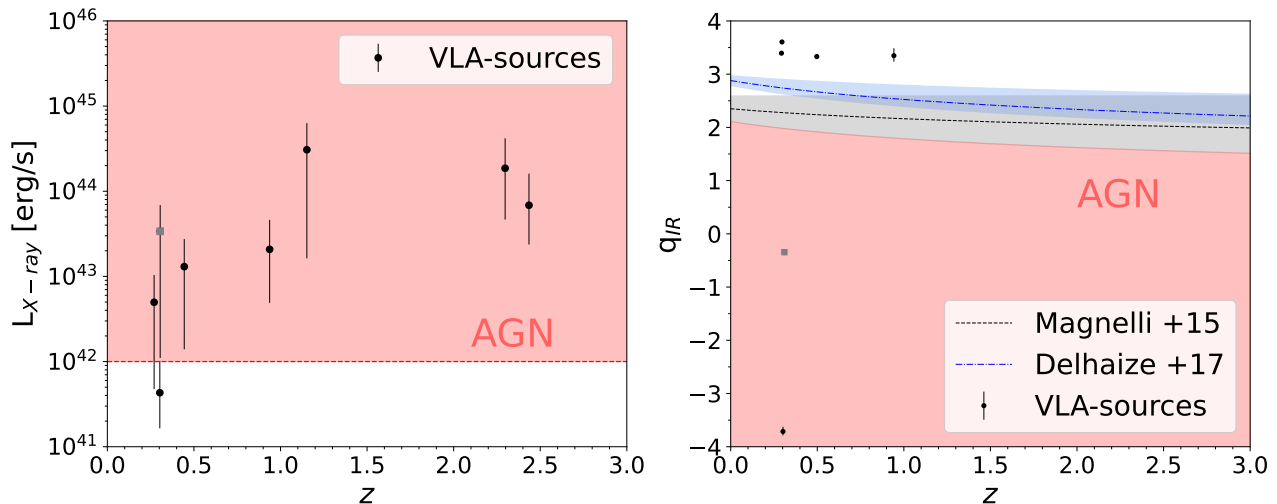


Figure 7. Left: X-ray luminosities of the VLA sources with X-ray counterparts. The red-shaded region shows the parameter space ($L_x > 10^{42}$ erg s $^{-1}$) dominated by AGN. Right: q_{IR} factor for the VLA radio sources with IR counterparts. The black dashed line shows the IRC reported by (Delhaize et al. 2017), and the grey shaded region indicates the 3σ uncertainty interval. The blue dotted line shows the IRC reported by (Magnelli et al. 2015), while the blue shaded region indicates the 3σ uncertainty interval. The gray data point correspond to the VLAHFF-J001426.56-302344.21 source which fulfill both criterion. The red-shaded region shows the parameter space (sources with radio excess) dominated by AGN. These procedures allow us to identify eight AGN candidates in the 6 GHz radio source catalog of A 2744.

UNCOVER survey by Wang et al. (2023). We can use the relation (Hopkins et al. 2003)

$$\left(\frac{\text{SFR}_u}{\text{M}_\odot \text{yr}^{-1}} \right) = \left(\frac{L_u}{1.81 \times 10^{21} \text{ W Hz}^{-1}} \right)^{1.186}, \quad (10)$$

where L_u is the u -band luminosity. This calibration is obtained using a sample of u -band luminosities derived from the SDSS K-corrected absolute u -band magnitudes (Blanton et al. 2003), also an obscuration correction based on the Balmer decrement and the extinction curve from Calzetti (2001) has been employed. Using this sample, the ordinary least-squares bisector method of linear regression (Isobe et al. 1990) is applied to $\log(L_U)$ and $\log(\text{SFR}_{H\alpha})$.

5.3.1. Comparing Unobscured and Obscured SFRs

We compare the three SFR estimates available for the 46 sources with *HST*, *JWST*, and VLA counterparts and redshift information: the SFR derived via SED fitting using optical/near-infrared data reported by the UNCOVER team (Wang et al. 2023), hereafter $\text{SFR}_{\text{UNCOVER}}$, the SFR derived from the u -band luminosity (SFR_u), and the SFR inferred from the 6 GHz flux density ($\text{SFR}_{6\text{GHz}}$).

When comparing the $\text{SFR}_{\text{UNCOVER}}$ with the $\text{SFR}_{6\text{GHz}}$ derived in this work (see the left panel of Figure 8), it is notable that our radio SFRs are higher, on average, by a factor 5. Such a discrepancy is mainly result from dust extinction in the optic/nir and u -band observations. The uncertainties can be attributed

to several factors, including the scatter in the SFRs calibrations. For instance, the stellar templates used by (Wang et al. 2023) to compute the estimated SFRs are particularly uncertain at high stellar masses and low metallicities. As observed in Figure 9, our sample is mainly composed of massive SFGs. More importantly, the discrepancy between $\text{SFR}_{\text{UNCOVER}}$ and $\text{SFR}_{6\text{GHz}}$ suggests that the correction for dust extinction applied during the SED fitting is insufficient to account for the star formation activity that is heavily obscured in our massive SFGs. This highlights the importance of radio observations as star formation tracers since they are not affected by dust attenuation.

A similar discrepancy is observed when we compare the $\text{SFR}_{6\text{GHz}}$ with those inferred from the rest-frame u -band luminosities reported in the UNCOVER catalog (see the bottom panel of Figure 8). The SFR_u are lower, on average, by a factor of 50. The discrepancy between the u -band and 6 GHz SFRs can arise from several factors. For example, the u -band luminosity can vary significantly during the stellar evolution, making it less reliable as an SFR tracer (Hopkins et al. 2003). Moreover, the average u -band obscuration correction ranges from a factor 3 at SFRs of $1 \text{ M}_\odot \text{yr}^{-1}$ up to about a factor 10 at SFRs of $100 \text{ M}_\odot \text{yr}^{-1}$. This, again, stresses the need for star formation tracers unaffected by dust, like radio continuum emission. Without the 6 GHz data, we would be underestimating the SFR of galaxies in our sample by a factor of 10, on average, because most of the star

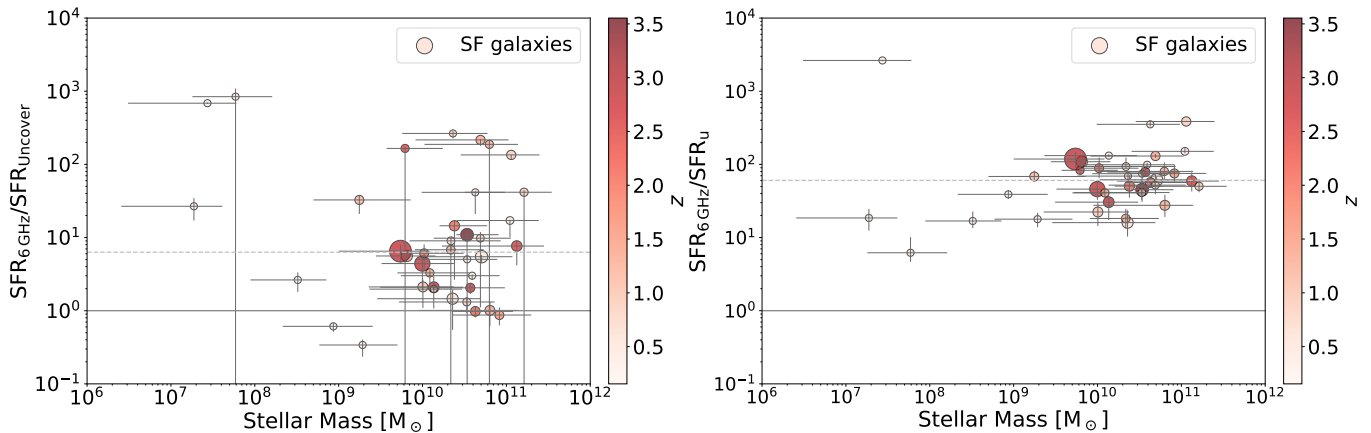


Figure 8. Left panel: ratio of the $\text{SFR}_{6\text{GHz}}$ to $\text{SFR}_{\text{Uncover}}$ as a function of stellar mass. Right panel: ratio of the $\text{SFR}_{6\text{GHz}}$ to SFR_u as a function of stellar mass. The magnification of each source is represented by the marker size; thus, larger markers indicate higher magnification. The color code represents the redshift, therefore the redder the marker the higher the redshift of the source. The solid horizontal lines are located at 1, i.e., where the radio and optical-near IR SFRs are equal. The horizontal dashed lines show the median ratios, indicating that 6 GHz SFR of galaxies in our sample are a factor 5-50, on average than u -band and optical-near IR SFRs.

formation out to $z \sim 5$ remains heavily obscured (e.g., Bouwens et al. 2020; Zavala et al. 2021).

Our $\text{SFR}_{6\text{GHz}}$ values are not free of uncertainties. Albeit we consider the uncertainties related to the spectral index for SFGs (typically 0.7 ± 0.1) and the 5% error floor in the z_{phot} imposed by (Weaver et al. 2024), several systematic uncertainties are contributing to the dispersion of the SFR *vs* radio luminosity calibration. For instance, no systematic errors in the empirical IR-radio correlation are being considered, nor are the uncertainties introduced by adopting a given IMF.

5.4. Galaxies in the Star Formation vs Stellar Mass Plane

We adopt the main sequence model proposed by Leslie et al. (2020) since they use radio-based SFRs of a large sample of \sim half-million galaxies in the COSMOS2015 catalog (Laigle et al. 2016). The model is described by

$$\log(\langle \text{SFR} \rangle) = S_o - a_1 t - \log \left(1 + \left(\frac{10^{M'_t}}{10^M} \right) \right), \quad M'_t = M_0 - a_2 t \quad (11)$$

where M is $\langle \log(M_*/M_\odot) \rangle$ and t is the age of the universe. For star-forming populations: $S_o = -2.97_{-0.09}^{+0.08}$, $M_0 = 11.06_{-0.16}^{+0.15}$, $a_1 = 0.22_{-0.01}^{+0.01}$, and $a_2 = 0.12_{-0.02}^{+0.03}$ (Leslie et al. 2020). Note that this model uses the Chabrier IMF as the UNCOVER and our calculated SFR values. The 46 VLA radio sources with *JWST/HST* counterparts are plotted in the logarithmic SFR-stellar mass diagram (see Figure 9). To compensate for the redshift dependence of the main sequence and visualization purposes we split our sample into three redshift bins: $0 < z \leq 1$, $1 < z \leq 2$, and $2 < z \leq 3.55$,

containing 20, 8, and 10 galaxies, respectively. As observed in Figure 9, SFGs preferentially lie at the massive end of the main sequence, while a minor fraction of low-mass ($\log(M_*/M_\odot) \lesssim 9$) starburst galaxies (i.e., above the main sequence) are also detected. This is a consequence of our detection limit, which imposes a minimum SFR (per redshift) that can be detected in our image. This leads to the detection of both low- and high-mass starbursts, as well as massive galaxies on the main sequence that harbor high SFRs. It is noteworthy that galaxies with higher magnification tend to have lower mass and SFR, emphasizing once again the importance of gravitational lensing for detecting fainter and more distant galaxies.

5.5. Radio Properties of Little Red Dots

A key discovery of the *JWST* is the abundant population of the so-called Little Red Dots (LRDs; e.g., Kocevski et al. 2023; Harikane et al. 2023; Labbe et al. 2024; Labbé et al. 2023; Barro et al. 2024; Kocevski et al. 2024). These are $z \gtrsim 4$ compact galaxies with red optical colors and even broad $\text{H}\alpha$ emission lines suggesting the presence of type I AGN (e.g., Greene et al. 2024; Matthee et al. 2024). Alternatively, LRDs could be compact starbursts with ionized outflows leading to emission line broadening (e.g., Wang et al. 2025). To gather a more complete view of the *JWST*-discovered LRDs, multi-frequency analysis have been implemented. Unexpectedly, it is found that the vast majority of LRDs are not detected in the deepest X-ray images (Yue et al. 2024; Ananna et al. 2024; Maiolino et al. 2025), which is in conflict with expectations from broad line AGN scaling relations. In this context, radio observations are

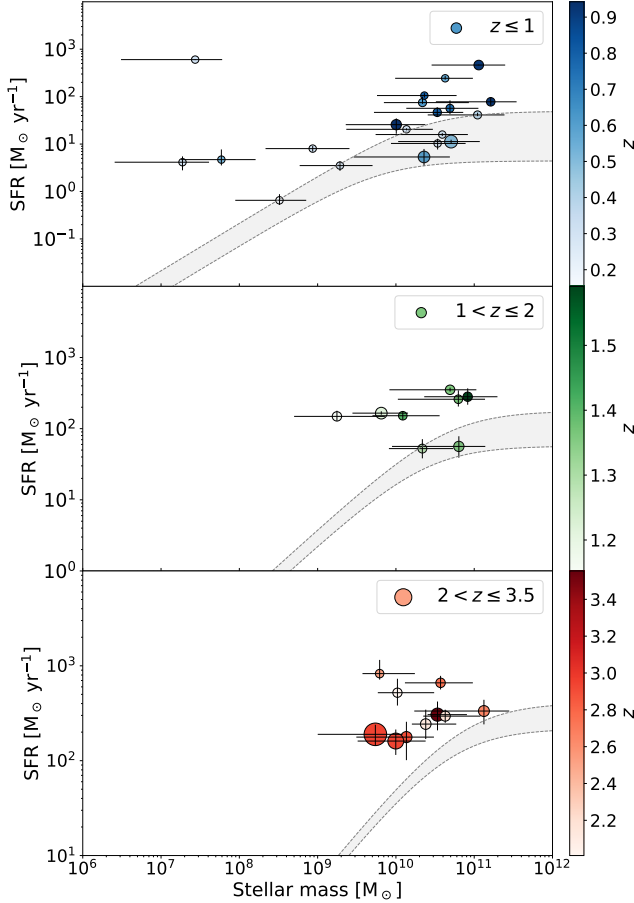


Figure 9. Sources in our sample in the SFR *vs* stellar mass plane. The SFRs shown is derived from the 6 GHz observations. From top to bottom, the first panel includes the sources with $0 \leq z \leq 1$, the second panel includes the sources with $1 < z \leq 2$, and the third panel includes sources with $2 < z \leq 3.55$. The gray region corresponds to the main sequence range between the lowest and highest z value of each panel. The magnification of each source is represented by the marker size; thus, larger markers indicate higher magnification. The AGN candidates are not plotted.

becoming relevant to trace the potential signatures of AGN processes. Several studies have looked for radio counterparts of LRDs identified in different cosmological fields (e.g., Mazzolari et al. 2024; Perger et al. 2025). Yet, only one LRD have been detected in radio (Gloude-mans et al. 2025): PRIMER-COS 3866 at $z = 4.66$.

Here, we crossmatch the catalog of LRDs reported by Kocevski et al. (2024) with our 6 GHz catalog of A 2744. Despite the gravitational lens created by the cluster that increases the likelihood of detecting these puzzling high- z sources, we find that none of the 23 LRDs in A 2744 are detected in our map above peak $\text{SNR} = 5$. A visual inspection does not reveal any tentative detection at the position of the LRDs. Af-

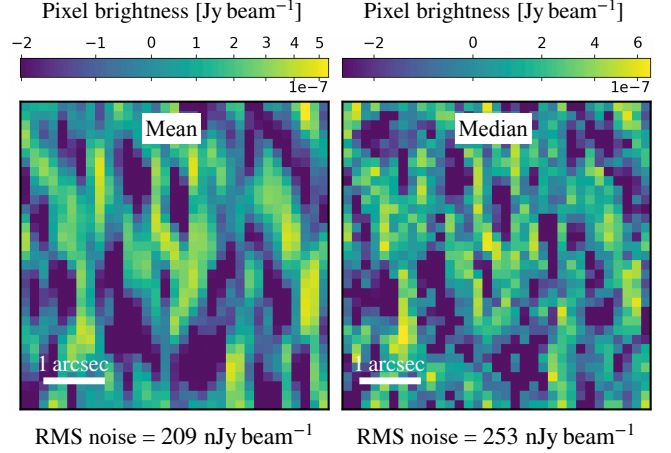


Figure 10. Mean and median stacked 6 GHz images at the position of the 23 LRDs in A 2744 reported by Kocevski et al. (2024). No signal has been detected down to an rms noise of $\approx 200 \text{ nJy beam}^{-1}$.

ter producing a stacked image of the 23 radio images, we find no significant detection. The resulting rms noise of the mean stacked image is $209 \text{ nJy beam}^{-1}$ (or $253 \text{ nJy beam}^{-1}$ if a median stack is adopted; see Figure 10). Since we are stacking lensed galaxies, we correct the rms noise values by lensing magnification by taking the mean (or median) μ value of the stacked galaxies, which is 1.95 (1.50). This leads to a 3σ limit to the observed 6 GHz radio emission of $\approx 600 \text{ nJy beam}^{-1}$ ($\approx 750 \text{ nJy beam}^{-1}$), which translates into a radio luminosity of $4.1 \times 10^{39} \text{ erg s}^{-1}$ ($6.7 \times 10^{39} \text{ erg s}^{-1}$) adopting the median redshift of the sample of $z \approx 6$ and a typical radio spectral index of $\alpha = 0.7$. This 3σ upper limit is comparable with that reported for LRDs in the COSMOS and GOODS fields whose radio luminosity at 1.3-5 GHz in the rest-frame is $\lesssim 2 \times 10^{39} \text{ erg s}^{-1}$ (Mazzolari et al. 2024; Gloude-mans et al. 2025). The expected radio luminosity of LRDs from constraints on their X-ray emission is $< 10^{37-39} \text{ erg s}^{-1}$ (see Section 5.1 of Gloude-mans et al. 2025). Since our upper limit to the radio luminosity of LRDs is still close/above the expected value, deeper observations are needed to provide robust constraints on the origin of LRDs and their potential AGN.

5.6. A Sample of Radio-selected, Moderately Lensed Galaxies in the Frontier Fields

A key goal of the VLA Frontier Fields project is to leverage gravitational lensing to detect high-redshift and/or intrinsically faint galaxies. On this regard, here we present a compilation of 22 moderately/strongly lensed galaxies (with $\mu \geq 2$) in the VLA Frontier Field project. 13 of such galaxies are found in the MACSJ0416.1-2403, MACSJ0717.5+3745, and

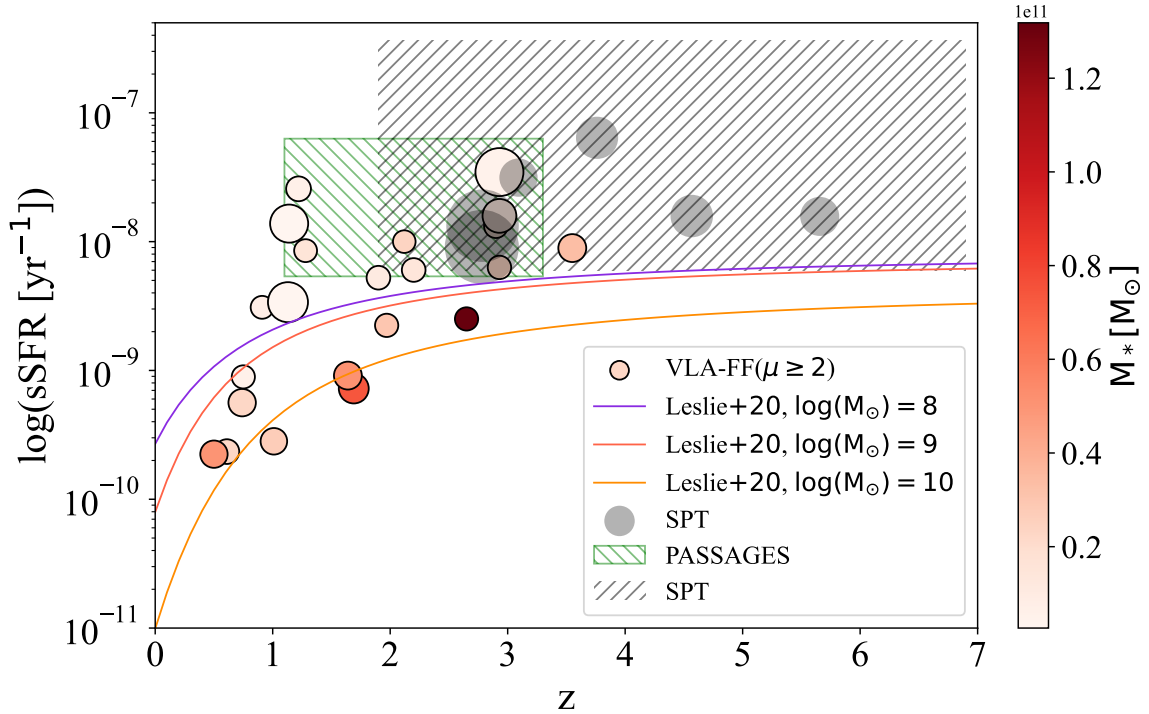


Figure 11. A sample of 22 moderately/strongly lensed ($\mu \geq 2$) sources from the VLA Frontier Fields program (Heywood et al. 2021, and this work) in the sSFR *vs* redshift plane. The gray hatched area shows the full sSFR– z range of galaxies in the SPT survey (Reuter et al. 2020), while the individual gray symbols mark the SPT galaxies reported by (Ma et al. 2015). The green hatched area indicates the sSFR– z range covered by the PASSAGES survey (Kamienski et al. 2024). Solid lines trace the sSFR evolution from (Leslie et al. 2020) for galaxies with three representative stellar masses. Marker size scales with stellar mass. Contrary to the well-studied PASSAGES and SPT samples, the radio-selected galaxies in the Frontier Fields span across a wide range of sSFR at $z \approx 1 - 2$, allowing us to probe both extreme starbursts and more typical, main sequence galaxies.

MACSJ1149.5+2223 fields (Heywood et al. 2021), while 9 lie in the A 2744 field (see Table 3.). The stellar mass and SFR range of this sample is $\log(M_*/M_\odot) \approx 9.4 - 11.2$ and $5.2 - 301 M_\odot \text{ year}^{-1}$, respectively, and span across a redshift and magnification range of $\approx 0.5 - 3.55$ and $\approx 2.06 - 9.27$ (see Table 3). These properties differ from those of strongly lensed galaxies in the well-studied PASSAGES (Planck All-Sky Survey to Analyze Gravitationally-lensed Extreme Starbursts) and South Pole Telescope (SPT) samples. The PASSAGES sample of 30 galaxies have median redshift of $\bar{z} \approx 2$ and $\overline{\text{SFR}} \approx 1500 M_\odot \text{ yr}^{-1}$ (e.g., Kamienski et al. 2024); while the 81 SPT-selected galaxies have, on average, higher redshifts and SFRs with median $\bar{z} \approx 3.9$ and $\overline{\text{SFR}} \approx 2300 M_\odot \text{ yr}^{-1}$ (e.g., Reuter et al. 2020; Liu et al. 2024). These systems, therefore, have been known as the most extreme starbursts at high redshifts.

To illustrate how our sample of 22 moderately/strongly lensed galaxies in the Frontier Fields compares with the SPT and PASSAGES samples, in Figure 11 we plot their specific SFR (sSFR) as a function of redshift. It is evident that the Frontier Fields sample exhibit lower sSFR and redshifts than the SPT and

PASSAGES samples. While the SPT and PASSAGES sample have opened a window into the star formation conditions of massive, starburst systems at $z \approx 2 - 7$ (e.g., Ma et al. 2015; Reuter et al. 2020), the Frontier Field sample presented here can be used to zoom into galaxy evolution processes of more typical, main sequence galaxies at the peak epoch of star formation in the Universe ($z \approx 1 - 2$).

6. SUMMARY

Using the VLA C-band receivers centered at 6 GHz, we generated the deepest ($\sim 1 \mu\text{Jy beam}^{-1}$), high resolution ($0''.82$) radio image to date of A 2744 —the third strongest lensing cluster from the six Hubble Frontier Fields. The main data products and results derived from this work are the following.

- The radio source catalog contains 93 sources detected with a peak SNR > 5 . Five of them are extended or multi-component sources and 88 are cataloged as point-like sources. The total fraction of spurious sources in our radio catalog is 16%.

- The sample has a median effective radius of $0''.27$ and 25th/75th percentiles of $0''.2/0''.5$, corresponding to a ~ 2.01 kpc at $z = 0.93$, and a median flux density of $15.6 \mu\text{Jy beam}^{-1}$ and 25th/75th percentiles of $11.2/33.4 \mu\text{Jy beam}^{-1}$.
- We cross-match our 6 GHz radio source catalog with the UNCOVER (Wang et al. 2023; Weaver et al. 2024) and DUALZ survey (Fujimoto et al. 2023). From the 70 sources present in the area where the footprints overlaps, we find 46 radio sources with a *JWST*, *HST* counterpart, and 20 of them are related to an ALMA 1.2 mm sources.
- Our sample is composed of galaxies in the redshift range $0.15 < z \leq 3.55$ with a median of $z_{\text{spec}} = 0.30$ and $z_{\text{phot}} = 1.07$, with 11 of them being moderately magnified (i.e., $1 \leq \mu \leq 9.27$). The stellar masses span from $6.6 \times 10^5 M_{\odot}$ to $1.6 \times 10^{11} M_{\odot}$. The median SFR from NIR/Optical photometry is $0.9_{-0.2}^{+1.7} M_{\odot}\text{yr}^{-1}$, the derived 6 GHz median SFR is $1.9_{-1.1}^{+0.8} M_{\odot}\text{yr}^{-1}$, excluding the AGN candidates, and the derived *u*-band based median SFR is $0.3_{-0.0}^{+0.9} M_{\odot}\text{yr}^{-1}$.
- We identified 9 AGN candidates using X-ray, IR, and radio diagnostics, leading to an AGN fraction in our sample of approximately 10-20%. This is consistent with the predicted value of around 14% derived from simulations and models by Mancuso et al. (2017) and Bonaldi et al. (2019).
- We compute dust obscured (rest-frame *u*-band) and un-obscured (radio) SFRs for 46 VLA sources with available redshift and *u*-band flux densities. The radio-based SFRs are a factor 5, on average, larger than those from *u*-band imaging. We also compare the 6 GHz SFRs with those reported by Weaver et al. (2024) using SED fitting of *JWST/HST* photometric data, revealing that the former are a factor 50 higher.
- None of the 23 LRDs at $z \approx 6$ reported by Gloude-mans et al. (2025) are detected in the 6 GHz map. After stacking, we derive a 3σ

upper limit to the 6 GHz radio luminosity of $4.1 \times 10^{39} \text{ erg s}^{-1}$.

- The 22 galaxies in the VLA Frontier Field survey that are moderately/strongly lensed ($\mu > 2$) probe a sSFR regime that has been largely missed by existing samples of strongly lensed galaxies, like PASSAGES and SPT, facilitating spatially resolved studies of star formation in more typical, main sequence galaxies at $z \approx 1 - 2$.

ACKNOWLEDGMENTS

E.A.O. and E.F.-J.A. acknowledge support from the Program to Support Research and Technological Innovation Projects (PAPIIT; Projects IA102023 and IA104725) of the National Autonomous University of Mexico (UNAM), and from the Program “Frontier Science” (Project ID CF-2023-I-506) of the National Council of Humanities, Sciences and Technologies (CONAHCyT). The National Radio Astronomy Observatory is a facility of the National Science Foundation operated under cooperative agreement by Associated Universities, Inc. E.A.O thanks the Hubble Frontier Fields Project team (PI: J. Lotz) for their observations that contributed to this work. Special thanks are extended to the “Ultradeep NIRSpc and NIRCcam Observations before the Epoch of Reionization” (UNCOVER) project team (PIs: Ivo Labbe & Rachel Bezanson) for providing the invaluable *HST* and *JWST* data and observations that were incorporated into this study. Finally, we acknowledge Fujimoto Seiji and collaborators for their observations at 1.2mm using ALMA, which were used in this work. IRS acknowledges the support of the Science and Technology Facilities Council (STFC) under grant ST/X001075/1.

Facilities: NSF’s Karl G. Jansky Very Large Array (VLA), *HST*, *JWST*, and ALMA.

Software: astropy (Robitaille et al. 2013), CASA (Bean et al. 2022), PyBDSF (Mohan & Rafferty 2015)

DATA AVAILABILITY

The VLA Frontier Fields survey is a public legacy project, and we make all our catalog and image products freely available at <https://science.nrao.edu/science/surveys/vla-ff>.

APPENDIX

A. TABLES AND RGB IMAGES

Here we present the tables with the positions, radio sizes, the flux densities of the 93 radio sources reported in this work. We report the redshifts, magnification factors, stellar masses, and star-formation rates derived from UNCOVER (Wang et al. 2023), as well as the sSFR and other properties of the moderately/strongly lensed ($\mu > 2$) galaxies from the SPT and VLA surveys. Additionally, we show RGB images from the 46 sources with *JWST* + *HST* counterparts, including VLAHFF-J001404.22-301920.31 and VLAHFF-J001415.59-302259.85 sources (see Figures 12 & 13).

Table 1. Flux densities, peak brightness, primary beam response, angular radio size, physical size and additional flags for the 93 radio sources.

N	ID	R.A. (deg)	Decl. (deg)	$S_{\text{tot}} (\mu\text{Jy})$	$S_{\text{peak}} (\mu\text{Jy})$	PBr (%)	θ_M (arcsec)	Physical Size (kpc)	R ^a	T ^b
1	VLAHFF-J001446.17-302710.35	3.692361	-30.452875	8766.96 ± 402.34	831.36 ± 8.63	10.7	68.03 ± 18.64	-	1	M
2	VLAHFF-J001441.26-302236.10	3.671925	-30.376694	21.53 ± 5.86	19.78 ± 3.14	30.1	0.61 ± 0.09	-	0	C
3	VLAHFF-J001440.32-302612.91	3.668003	-30.436919	82.75 ± 12.17	41.11 ± 3.87	25.4	2.51 ± 0.29	-	1	M
4	VLAHFF-J001440.29-302216.56	3.667856	-30.371267	48.57 ± 11.35	19.66 ± 3.00	31.9	0.00 ± 0.06	-	0	C
5	VLAHFF-J001439.41-302821.31	3.664227	-30.472586	1553.00 ± 101.56	233.36 ± 12.28	8.1	3.15 ± 0.18	-	1	M
6	VLAHFF-J001438.81-302717.69	3.661706	-30.454913	66.98 ± 10.08	56.11 ± 5.14	19.2	0.52 ± 0.04	-	0	C
7	VLAHFF-J001438.70-302247.65	3.661242	-30.379903	39.43 ± 4.73	32.68 ± 2.39	41.7	0.60 ± 0.04	-	1	C
8	VLAHFF-J001438.01-302118.43	3.658372	-30.355120	16.46 ± 5.13	16.95 ± 2.79	31.6	0.00 ± 0.14	-	0	C
9	VLAHFF-J001437.61-302611.93	3.656724	-30.436647	47.61 ± 5.57	40.68 ± 2.87	34.7	0.00 ± 0.10	0.00 ± 0.24	0	C
10	VLAHFF-J001437.47-302315.32	3.656126	-30.387590	52.89 ± 3.40	53.45 ± 1.97	49.2	0.00 ± 0.01	-	0	C
11	VLAHFF-J001437.16-302249.66	3.654828	-30.380460	10.13 ± 2.92	12.32 ± 1.75	48.6	0.00 ± 0.10	-	0	C
12	VLAHFF-J001434.50-302750.89	3.643730	-30.464137	204.02 ± 8.55	177.33 ± 4.49	22.5	0.37 ± 0.01	-	1	C
13	VLAHFF-J001433.38-302233.10	3.639099	-30.375860	297.95 ± 5.34	244.89 ± 1.60	62.8	0.47 ± 0.00	-	1	C
14	VLAHFF-J001432.82-302931.41	3.636745	-30.492057	317.23 ± 86.25	79.66 ± 17.66	5.6	1.51 ± 0.28	-	1	C
15	VLAHFF-J001432.50-302744.59	3.635416	-30.462386	55.53 ± 6.65	50.65 ± 3.61	28.1	0.32 ± 0.03	-	1	C
16	VLAHFF-J001432.23-302615.72	3.634283	-30.437699	23.13 ± 4.24	17.43 ± 2.02	52.6	0.50 ± 0.05	1.66 ± 0.16	0	C
17	VLAHFF-J001430.84-302427.78	3.628485	-30.407716	78.34 ± 5.48	24.72 ± 1.35	77.9	1.58 ± 0.08	3.39 ± 0.17	1	C
18	VLAHFF-J001430.20-302929.77	3.625825	-30.491602	115.59 ± 21.09	116.14 ± 11.90	8.1	0.00 ± 0.05	-	0	C
19	VLAHFF-J001429.51-302080.48	3.622937	-30.335689	37.87 ± 5.45	32.10 ± 2.81	37.7	0.42 ± 0.04	-	1	C
20	VLAHFF-J001428.61-302270.98	3.619209	-30.368883	7.35 ± 2.53	6.75 ± 1.26	74.8	0.00 ± 0.21	0.00 ± 0.00	0	C
21	VLAHFF-J001428.50-302334.57	3.618741	-30.392937	23.33 ± 4.34	8.22 ± 1.15	87.6	1.90 ± 0.28	3.50 ± 0.00	1	C
22	VLAHFF-J001428.24-301870.79	3.617655	-30.302163	151.87 ± 42.09	56.96 ± 11.90	9.0	1.32 ± 0.24	-	1	C
23	VLAHFF-J001427.96-302940.64	3.616519	-30.484623	75.81 ± 23.07	33.21 ± 7.38	14.8	1.00 ± 0.18	-	0	C
24	VLAHFF-J001427.54-302643.08	3.614737	-30.445299	36.54 ± 7.88	10.26 ± 1.80	57.1	0.00 ± 0.08	0.00 ± 0.14	0	C
25	VLAHFF-J001426.84-302518.28	3.611852	-30.421745	164.32 ± 2.29	155.90 ± 1.28	82.6	0.23 ± 0.00	0.73 ± 0.01	1	C
26	VLAHFF-J001426.56-302344.21	3.610655	-30.395614	117.71 ± 7.34	71.50 ± 1.12	93.3	0.65 ± 0.01	1.10 ± 0.01	1	C
27	VLAHFF-J001426.59-302631.78	3.610780	-30.442160	53.28 ± 3.12	48.30 ± 1.69	62.6	0.35 ± 0.01	0.60 ± 0.02	1	C
28	VLAHFF-J001426.07-302452.48	3.608642	-30.414576	13.91 ± 3.10	8.52 ± 1.27	89.2	0.68 ± 0.08	2.24 ± 0.26	0	C
29	VLAHFF-J001425.35-302550.30	3.605633	-30.418138	6.28 ± 2.10	6.14 ± 1.15	88.4	0.00 ± 0.11	0.00 ± 0.37	0	C
30	VLAHFF-J001424.09-302346.25	3.600380	-30.396179	9.98 ± 2.88	5.26 ± 1.09	98.0	0.00 ± 0.05	0.00 ± 0.17	0	C
31	VLAHFF-J001423.98-301813.54	3.599906	-30.303762	88.52 ± 16.06	78.39 ± 8.44	12.2	0.00 ± 0.05	-	0	C
32	VLAHFF-J001423.78-302135.10	3.599074	-30.359751	14.51 ± 3.73	8.39 ± 1.44	75.1	1.15 ± 0.19	4.00 ± 0.67	1	C
33	VLAHFF-J001423.50-302017.36	3.597914	-30.338156	19.20 ± 4.85	14.14 ± 2.26	48.7	0.63 ± 0.08	-	0	C
34	VLAHFF-J001422.76-302329.90	3.594818	-30.391639	11.46 ± 3.14	6.64 ± 1.09	98.8	0.00 ± 0.03	0.00 ± 0.05	0	C
35	VLAHFF-J001422.39-302330.70	3.593276	-30.384361	45.43 ± 2.66	31.20 ± 1.19	96.6	0.59 ± 0.02	1.06 ± 0.03	1	C
36	VLAHFF-J001422.18-302655.54	3.592419	-30.448761	20.79 ± 2.85	22.65 ± 1.74	59.1	0.00 ± 0.03	-	0	C
37	VLAHFF-J001422.03-302149.70	3.591772	-30.363805	49.76 ± 2.47	45.03 ± 1.33	80.7	0.44 ± 0.01	1.51 ± 0.04	1	C
38	VLAHFF-J001421.68-302410.26	3.590341	-30.400349	30.04 ± 2.34	23.26 ± 1.13	99.8	0.57 ± 0.02	1.43 ± 0.06	1	C
39	VLAHFF-J001420.63-302670.42	3.585977	-30.435396	1523.85 ± 30.80	615.45 ± 1.70	76.8	14.72 ± 0.47	27.79 ± 0.90	1	M
40	VLAHFF-J001421.04-302346.96	3.587683	-30.396379	21.77 ± 2.45	15.92 ± 1.14	100.0	0.65 ± 0.04	1.19 ± 0.07	1	C
41	VLAHFF-J001420.99-302216.54	3.587452	-30.371260	31.43 ± 2.59	24.47 ± 1.26	88.1	0.50 ± 0.02	1.53 ± 0.06	1	C
42	VLAHFF-J001420.72-302645.10	3.586354	-30.445860	15.48 ± 2.62	17.48 ± 1.60	62.9	0.00 ± 0.04	-	0	C
43	VLAHFF-J001420.70-302400.53	3.586244	-30.400148	9.80 ± 1.86	9.81 ± 1.04	99.8	0.00 ± 0.06	0.00 ± 0.10	0	C
44	VLAHFF-J001420.38-302838.04	3.584899	-30.477232	51.53 ± 7.52	48.86 ± 4.16	24.7	0.00 ± 0.04	-	0	C
45	VLAHFF-J001420.15-301925.08	3.583937	-30.323634	23.50 ± 6.18	21.30 ± 3.28	31.5	0.00 ± 0.08	-	0	C
46	VLAHFF-J001419.80-302370.61	3.582483	-30.385447	11.29 ± 2.60	7.77 ± 1.14	97.0	0.95 ± 0.13	3.04 ± 0.42	0	C
47	VLAHFF-J001419.51-302248.98	3.581301	-30.380272	9.66 ± 2.45	6.62 ± 0.95	94.1	0.00 ± 0.31	0.00 ± 0.94	0	C
48	VLAHFF-J001419.42-302326.84	3.580926	-30.390789	59.95 ± 2.47	44.17 ± 1.16	98.5	0.58 ± 0.01	0.00 ± 0.02	1	C

Table 1 continued

Table 1 (continued)

N	ID	R.A. (deg)	Decl. (deg)	$S_{\text{tot}} (\mu\text{Jy})$	$S_{\text{peak}} (\mu\text{Jy})$	PBr (%)	θ_M (arcsec)	Physical Size (kpc)	R ^a	T ^b
49	VLAHFF-J001418.89-302151.00	3.578714	-30.364165	3.65 ± 1.22	7.05 ± 0.98	80.1	0.00 ± 0.06	0.00 ± 0.16	0	C
50	VLAHFF-J001417.64-302960.15	3.573493	-30.485042	37.04 ± 10.75	36.62 ± 5.87	16.5	0.00 ± 0.11	-	0	C
51	VLAHFF-J001417.58-302300.58	3.573264	-30.383493	45.51 ± 2.02	44.35 ± 1.14	93.6	0.00 ± 0.01	0.00 ± 0.03	0	C
52	VLAHFF-J001416.55-302490.96	3.568938	-30.402765	16.22 ± 2.00	15.55 ± 1.12	94.4	0.00 ± 0.03	0.00 ± 0.11	0	C
53	VLAHFF-J001415.60-302444.11	3.564999	-30.412253	7.47 ± 1.79	8.63 ± 1.07	88.8	0.00 ± 0.07	0.00 ± 0.25	0	C
54	VLAHFF-J001415.59-302259.85	3.564970	-30.383291	7.75 ± 2.67	5.69 ± 1.24	89.3	0.70 ± 0.13	-	0	C
55	VLAHFF-J001415.32-302230.45	3.563831	-30.367624	9.37 ± 2.66	8.02 ± 1.36	77.7	0.00 ± 0.10	0.00 ± 0.33	0	C
56	VLAHFF-J001414.53-302458.17	3.560541	-30.416158	13.42 ± 3.38	7.87 ± 1.34	83.8	0.87 ± 0.12	2.93 ± 0.42	0	C
57	VLAHFF-J001414.43-302530.24	3.560129	-30.417568	16.22 ± 1.83	19.59 ± 1.19	82.7	0.00 ± 0.02	0.00 ± 0.08	0	C
58	VLAHFF-J001414.38-302240.05	3.559935	-30.377792	32.13 ± 2.34	29.59 ± 1.28	83.1	0.30 ± 0.02	0.70 ± 0.04	1	C
59	VLAHFF-J001414.42-302990.51	3.560099	-30.485974	64.74 ± 16.43	47.21 ± 7.26	13.7	0.00 ± 0.18	-	0	C
60	VLAHFF-J001413.99-302234.11	3.558298	-30.376141	7.84 ± 2.03	8.65 ± 1.21	80.9	0.00 ± 0.07	0.00 ± 0.08	0	C
61	VLAHFF-J001413.96-302553.39	3.558179	-30.431496	17.13 ± 2.84	15.36 ± 1.50	69.9	0.00 ± 0.05	-	0	C
62	VLAHFF-J001413.92-302237.95	3.557983	-30.377208	26.80 ± 5.10	8.39 ± 1.23	81.3	2.01 ± 0.31	6.41 ± 0.98	1	C
63	VLAHFF-J001413.76-302556.47	3.557328	-30.432352	15.42 ± 3.52	10.78 ± 1.56	68.6	0.94 ± 0.13	-	0	C
64	VLAHFF-J001413.11-302660.34	3.554638	-30.435095	18.89 ± 4.56	10.16 ± 1.67	64.1	1.24 ± 0.20	-	1	C
65	VLAHFF-J001412.59-302523.48	3.552455	-30.423190	17.31 ± 5.29	6.31 ± 1.45	73.1	1.59 ± 0.35	-	1	C
66	VLAHFF-J001412.38-302611.10	3.551580	-30.436416	13.97 ± 3.19	12.80 ± 1.73	60.7	0.00 ± 0.06	-	0	C
67	VLAHFF-J001412.17-302928.31	3.550728	-30.491197	1558.60 ± 148.62	599.74 ± 12.64	8.4	8.02 ± 2.20	-	1	M
68	VLAHFF-J001411.80-302180.11	3.549159	-30.352254	13.68 ± 4.47	9.52 ± 1.97	53.1	0.00 ± 0.18	0.00 ± 0.59	0	C
69	VLAHFF-J001411.58-301956.18	3.548262	-30.332271	14.42 ± 4.57	17.76 ± 2.86	31.6	0.00 ± 0.09	0.00 ± 0.28	0	C
70	VLAHFF-J001411.38-302317.88	3.547433	-30.388300	19.00 ± 2.42	17.84 ± 1.34	77.6	0.32 ± 0.03	1.05 ± 0.09	1	C
71	VLAHFF-J001411.20-302358.86	3.546673	-30.399682	16.83 ± 3.16	11.46 ± 1.40	78.1	0.63 ± 0.06	1.94 ± 0.18	0	C
72	VLAHFF-J001410.53-302420.03	3.543875	-30.405564	13.31 ± 3.24	9.30 ± 1.46	74.4	0.69 ± 0.09	-	0	C
73	VLAHFF-J001409.67-302770.09	3.540288	-30.451968	12.69 ± 3.48	17.49 ± 2.35	37.5	0.00 ± 0.07	-	0	C
74	VLAHFF-J001409.49-302135.29	3.539524	-30.359802	30.05 ± 4.05	23.76 ± 1.99	53.0	0.50 ± 0.04	1.69 ± 0.12	1	C
75	VLAHFF-J001409.39-302136.85	3.539136	-30.360236	28.65 ± 7.92	8.98 ± 1.94	53.0	1.67 ± 0.34	5.73 ± 1.15	1	C
76	VLAHFF-J001409.33-302856.00	3.538884	-30.482222	170.09 ± 17.40	146.90 ± 9.04	11.4	0.00 ± 0.03	-	0	C
77	VLAHFF-J001409.18-302055.86	3.538244	-30.348849	29.75 ± 6.26	17.85 ± 2.51	42.1	0.97 ± 0.12	3.34 ± 0.42	1	C
78	VLAHFF-J001409.12-302460.81	3.538019	-30.401892	11.69 ± 3.63	7.30 ± 1.45	69.1	0.00 ± 0.26	-	0	C
79	VLAHFF-J001408.91-302114.10	3.537107	-30.353916	21.60 ± 3.62	22.59 ± 2.08	45.9	0.00 ± 0.05	0.00 ± 0.00	0	C
80	VLAHFF-J001408.71-302137.38	3.536279	-30.360385	26.71 ± 5.30	15.95 ± 2.13	50.7	0.80 ± 0.09	2.79 ± 0.30	1	C
81	VLAHFF-J001408.30-302415.55	3.534563	-30.404319	30.69 ± 3.01	27.01 ± 1.59	65.1	0.48 ± 0.03	-	1	C
82	VLAHFF-J001408.14-302429.57	3.533905	-30.408214	15.66 ± 4.23	9.48 ± 1.72	63.4	0.76 ± 0.11	-	0	C
83	VLAHFF-J001407.66-302436.05	3.531934	-30.410013	10.04 ± 2.70	10.75 ± 1.57	60.8	0.00 ± 0.08	-	0	C
84	VLAHFF-J001406.17-301947.83	3.525705	-30.329951	22.47 ± 6.22	33.86 ± 4.37	18.6	0.00 ± 0.06	-	0	C
85	VLAHFF-J001405.71-302217.28	3.523780	-30.371467	15.61 ± 4.31	12.99 ± 2.20	46.5	0.47 ± 0.07	1.60 ± 0.24	0	C
86	VLAHFF-J001405.35-302358.26	3.522276	-30.399516	28.42 ± 3.31	28.03 ± 1.87	52.1	0.00 ± 0.03	-	0	C
87	VLAHFF-J001405.29-302042.41	3.522059	-30.345113	23.30 ± 6.60	21.40 ± 3.60	27.5	0.36 ± 0.07	1.09 ± 0.20	0	C
88	VLAHFF-J001405.17-302755.12	3.521556	-30.465311	38.22 ± 12.32	32.09 ± 6.25	16.1	0.00 ± 0.1	-	0	C
89	VLAHFF-J001404.74-302451.09	3.519756	-30.414192	20.80 ± 5.40	13.38 ± 2.29	46.3	0.73 ± 0.10	-	0	C
90	VLAHFF-J001404.36-302448.48	3.518187	-30.413466	540.40 ± 8.34	482.78 ± 2.19	44.9	0.44 ± 0.00	-	1	C
91	VLAHFF-J001404.22-301920.31	3.517602	-30.322308	50.07 ± 15.52	51.86 ± 8.38	10.2	0.00 ± 0.15	-	0	C
92	VLAHFF-J001400.02-302045.41	3.500070	-30.345947	161.45 ± 12.74	145.49 ± 6.85	13.9	0.40 ± 0.02	1.07 ± 0.05	1	C
93	VLAHFF-J001359.10-302417.60	3.496248	-30.404889	37.91 ± 11.90	17.69 ± 3.96	24.9	1.20 ± 0.24	-	0	C

NOTE—**References**—^aIf the sources are confidently resolved along the major axis ($\phi_M - \theta_{1/2} \geq 2\sigma_{\phi_M}$), R = 1. Else, if $\phi_M - \theta_{1/2} < 2\sigma_{\phi_M}$, R=0. ^bT=C for compact single sources and T=M for multi-component, and extended complex radio sources.

Table 2. Spectroscopic and photometric redshifts, magnifications, stellar masses, metallicities, 1.2 mm fluxes and AGN flagg for the 46 radio sources with counterparts.

VLA ID	z_{spec}	z_{phot}	μ	M_* ($\log(M_*/M_\odot)$)	SFR_{NIR} ($M_\odot \text{yr}^{-1}$)	$\text{SFR}_{6 \text{ GHz}}$ ($M_\odot \text{yr}^{-1}$)	$S_{1.2\text{mm}}$ (μJy)	AGN
VLAHFF-J001437.61-302611.93	-	$0.621^{+0.27}_{-0.19}$	1.202	$10.34^{+0.46}_{-0.17}$	$08.30^{+15.26}_{-06.81}$	74.84 ± 10.63	-	0
VLAHFF-J001432.23-302615.72	-	$2.519^{+0.62}_{-0.56}$	1.311	$09.79^{+0.26}_{-0.40}$	$05.01^{+31.27}_{-04.75}$	827.62 ± 198.89	-	0
VLAHFF-J001430.84-302427.78	-	$0.382^{+0.05}_{-0.06}$	1.183	$11.04^{+0.07}_{-0.11}$	$02.41^{+0.19}_{-0.07}$	41.16 ± 03.44	-	0
VLAHFF-J001428.61-302270.98	-	$0.606^{+0.03}_{-0.04}$	2.462	$10.36^{+0.06}_{-0.06}$	$03.66^{+0.71}_{-0.58}$	5.35 ± 2.23	-	0
VLAHFF-J001428.50-302334.57	0.302	$0.107^{+0.01}_{-0.02}$	1.000	$08.95^{+0.14}_{-0.16}$	$00.04^{+0.04}_{-0.02}$	08.51 ± 01.88	-	1
VLAHFF-J001427.54-302643.08	0.269	$0.285^{+0.03}_{-0.03}$	1.000	$10.53^{+0.11}_{-0.12}$	$02.05^{+0.29}_{-0.68}$	10.31 ± 02.63	-	0
VLAHFF-J001426.84-302518.28	-	$0.923^{+0.10}_{-0.08}$	1.687	$11.06^{+0.07}_{-0.13}$	$03.44^{+16.06}_{-03.08}$	463.34 ± 07.98	-	0
VLAHFF-J001426.56-302344.21	0.305	$0.009^{+0.00}_{-0.00}$	1.000	$*05.89^{+0.13}_{-0.07}$	$89.83^{+103.64}_{-52.18} \times 10^{-6}$	43.99 ± 03.26	-	1
VLAHFF-J001426.59-302631.78	0.270	$0.283^{+0.04}_{-0.03}$	1.000	$09.40^{+0.13}_{-0.15}$	$00.20^{+0.21}_{-0.12}$	15.10 ± 01.05	-	1
VLAHFF-J001426.07-302452.48	-	$2.647^{+0.08}_{-0.07}$	2.180	$11.12^{+0.03}_{-0.06}$	$43.58^{+21.10}_{-17.20}$	333.69 ± 97.88	547 ± 52	0
VLAHFF-J001425.35-302550.30	-	$2.899^{+0.02}_{-0.05}$	2.262	$10.13^{+0.10}_{-0.11}$	$84.63^{+08.82}_{-10.01}$	177.24 ± 78.60	277 ± 53	0
VLAHFF-J001424.09-302346.25	0.943	$0.901^{+0.04}_{-0.06}$	1.939	$10.00^{+0.13}_{-0.17}$	$12.14^{+0.79}_{-0.17}$	25.66 ± 09.15	175 ± 34	0
VLAHFF-J001423.78-302135.10	-	$1.627^{+0.03}_{-0.04}$	1.411	$10.52^{+0.16}_{-0.15}$	$255.21^{+36.820}_{-139.21}$	180.79 ± 59.25	682 ± 56	1
VLAHFF-J001422.76-302329.90	0.301	$0.432^{+0.01}_{-0.00}$	1.000	$*07.27^{+0.08}_{-0.06}$	$00.16^{+0.01}_{-0.02}$	4.15 ± 01.35	-	0
VLAHFF-J001422.39-302330.70	0.296	$0.323^{+0.05}_{-0.02}$	1.000	$10.59^{+0.05}_{-0.06}$	$05.28^{+03.43}_{-02.42}$	15.88 ± 01.10	166 ± 51	0
VLAHFF-J001422.03-302149.70	-	$1.359^{+1.44}_{-1.29}$	1.645	$10.69^{+10.76}_{-10.61}$	$01.63^{+05.37}_{-00.52}$	351.90 ± 21.97	-	0
VLAHFF-J001421.68-302410.26	0.497	$0.509^{+0.06}_{-0.07}$	3.010	$10.70^{+0.13}_{-0.10}$	$02.07^{+01.37}_{-00.96}$	11.30 ± 01.06	175 ± 44	0
VLAHFF-J001420.63-302670.42	0.313	$0.985^{+0.01}_{-0.01}$	1.000	$*07.44^{+0.08}_{-0.06}$	$00.88^{+00.06}_{-00.06}$	603.59 ± 14.50	-	0
VLAHFF-J001421.04-302346.96	0.303	$4.175^{+0.16}_{-0.13}$	1.000	$08.94^{+0.29}_{-0.13}$	$13.13^{+02.15}_{-02.15}$	08.02 ± 01.07	-	0
VLAHFF-J001420.99-302216.54	-	$0.795^{+0.06}_{-0.03}$	1.000	$10.36^{+0.20}_{-0.12}$	$00.40^{+00.25}_{-00.14}$	105.41 ± 10.65	-	0
VLAHFF-J001420.70-302400.53	0.300	$3.237^{+0.14}_{-0.10}$	1.000	$09.29^{+0.00}_{-0.16}$	$10.35^{+02.77}_{-02.26}$	03.52 ± 00.79	-	0
VLAHFF-J001419.80-302370.61	-	$2.934^{+0.08}_{-0.07}$	4.597	$10.00^{+0.15}_{-0.17}$	$36.51^{+15.71}_{-17.59}$	160.99 ± 49.24	1491 ± 60	0
VLAHFF-J001419.51-302248.98	-	$3.554^{+0.16}_{-0.11}$	3.140	$10.53^{+0.14}_{-0.60}$	$27.97^{+18.22}_{-11.62}$	305.68 ± 104.23	330 ± 51	0
VLAHFF-J001419.42-302326.84	0.293	$0.366^{+0.04}_{-0.03}$	1.000	$10.13^{+0.07}_{-0.08}$	$10.37^{+13.27}_{-03.05}$	20.47 ± 01.00	286 ± 52	0
VLAHFF-J001418.89-302151.00	-	$0.526^{+0.11}_{-0.10}$	1.000	$*07.77^{+0.16}_{-0.24}$	$0.01^{+0.00}_{-0.01}$	04.70 ± 01.90	-	0
VLAHFF-J001417.58-302300.58	-	$1.217^{+0.05}_{-0.07}$	2.485	$09.81^{+0.08}_{-0.24}$	$29.51^{+04.40}_{-03.76}$	165.28 ± 09.17	913 ± 61	0
VLAHFF-J001416.55-302490.96	-	$2.175^{+0.05}_{-0.07}$	1.861	$10.63^{+0.26}_{-0.32}$	$301.39^{+44.47}_{-37.01}$	294.92 ± 47.28	293 ± 53	0
VLAHFF-J001415.60-302444.11	-	$1.279^{+0.10}_{-0.06}$	1.441	$10.34^{+0.17}_{-0.21}$	$7.70^{+20.74}_{-06.32}$	52.44 ± 15.77	275 ± 53	0
VLAHFF-J001415.32-302230.45	-	$1.358^{+0.05}_{-0.09}$	1.934	$10.80^{+0.07}_{-0.06}$	$55.76^{+14.40}_{-11.83}$	56.29 ± 20.10	263 ± 49	0
VLAHFF-J001414.53-302458.17	-	$2.297^{+0.04}_{-0.05}$	1.395	$10.89^{+0.05}_{-0.12}$	$59.77^{+36.66}_{-23.27}$	367.68 ± 120.51	-	1
VLAHFF-J001414.43-302530.24	-	$1.405^{+0.10}_{-0.08}$	1.341	$10.09^{+0.29}_{-0.23}$	$46.19^{+51.94}_{-25.12}$	151.94 ± 21.63	-	0
VLAHFF-J001414.38-302240.05	-	$0.444^{+0.01}_{-0.00}$	1.000	$*07.36^{+0.04}_{-0.02}$	$0.79^{+0.02}_{-0.02}$	28.06 ± 02.45	-	1
VLAHFF-J001413.99-302234.11	-	$0.154^{+0.01}_{-0.02}$	1.000	$08.51^{+0.08}_{-0.14}$	$0.25^{+0.07}_{-0.09}$	00.08 ± 00.02	-	0
VLAHFF-J001413.92-302237.95	-	$2.935^{+0.05}_{-2.04}$	9.272	$09.74^{+0.07}_{-0.10}$	$29.12^{+05.01}_{-05.24}$	189.58 ± 47.88	3.79 ± 57	0
VLAHFF-J001411.80-302180.11	-	$2.435^{+0.12}_{-0.16}$	1.483	$10.41^{+0.18}_{-0.16}$	$194.99^{+46.94}_{-52.49}$	401.11 ± 171.61	1871 ± 71	1
VLAHFF-J001411.58-301956.18	-	$0.937^{+0.17}_{-0.13}$	1.205	$11.14^{+0.08}_{-0.12}$	$1.34^{+06.76}_{-01.15}$	58.91 ± 23.07	-	1
VLAHFF-J001411.38-302317.88	-	$2.748^{+0.12}_{-0.15}$	1.632	$10.57^{+0.20}_{-0.19}$	$321.78^{+73.39}_{-52.76}$	661.54 ± 111.00	2815 ± 74	0
VLAHFF-J001411.20-302358.86	-	$0.807^{+0.07}_{-0.05}$	1.256	$10.53^{+0.06}_{-0.08}$	$35.37^{+00.65}_{-00.26}$	46.54 ± 10.72	-	0
VLAHFF-J001409.49-302135.29	-	$1.152^{+0.09}_{-0.09}$	1.606	$09.25^{+0.50}_{-0.15}$	$4.55^{+01.22}_{-02.79}$	148.78 ± 25.03	-	0
VLAHFF-J001409.39-302136.85	-	$2.009^{+0.11}_{-0.24}$	1.558	$10.02^{+0.29}_{-0.36}$	$85.42^{+20.68}_{-32.18}$	520.65 ± 185.91	596 ± 57	0
VLAHFF-J001409.18-302055.86	-	$1.362^{+1.50}_{-1.23}$	1.342	$10.80^{+0.07}_{-0.08}$	$1.38^{+02.38}_{-01.13}$	259.10 ± 68.75	-	0
VLAHFF-J001408.91-302114.10	-	$0.925^{+0.09}_{-0.07}$	1.326	$11.21^{+0.06}_{-0.10}$	$1.87^{+05.61}_{-01.64}$	77.81 ± 16.08	-	0
VLAHFF-J001408.71-302137.38	-	$1.591^{+0.15}_{-0.07}$	1.587	$10.92^{+0.14}_{-0.14}$	$321.88^{+51.67}_{-58.19}$	280.93 ± 70.92	2677 ± 88	0
VLAHFF-J001405.71-302217.28	-	$2.122^{+0.15}_{-0.14}$	2.057	$10.38^{+0.16}_{-0.47}$	$16.78^{+05.01}_{-10.54}$	243.16 ± 87.07	330 ± 57	0
VLAHFF-J001405.29-302042.41	-	$0.740^{+0.10}_{-0.10}$	1.167	$10.69^{+0.12}_{-0.14}$	$5.80^{+06.94}_{-04.18}$	56.77 ± 19.66	-	0
VLAHFF-J001400.02-302045.41	-	$0.563^{+0.07}_{-0.08}$	1.000	$10.63^{+0.10}_{-0.11}$	$5.87^{+08.35}_{-05.09}$	243.61 ± 23.25	-	0

Table 2 continued

Table 2 (continued)

VLA ID	z_{spec}	z_{phot}	μ	M_* ($\log(M_*/M_\odot)$)	SFR_{NIR} ($M_\odot \text{yr}^{-1}$)	$\text{SFR}_{6\text{ GHz}}$ ($M_\odot \text{yr}^{-1}$)	$S_{1.2\text{mm}}$ (μJy)	AGN
--------	-------------------	-------------------	-------	-------------------------------	--	--	---------------------------------------	-----

NOTE—VLA 6 GHz radio sources with counterparts in *JWST/HST/ALMA* imaging. The values of redshift, magnification, stellar mass, SFR, and metallicity are reported in the new release of UNCOVER by Wang et al. (2023), the upper and lower limits correspond to the 16th and 84th percentiles. The ALMA 1.2 mm fluxes are from Fujimoto et al. (2023). Additionally, the radio SFR from the 6 GHz image derived in this work (see section 5.3) with their respective errors are shown. Finally, in the last column, the AGN candidates are flagged with 1. * Values marked should be interpreted with caution, as they are not considered reliable—particularly for low-mass galaxies ($\log(M_*/M_\odot) < 8$) at low redshift ($0 < z < 1$).

Source Name ID	z	z_{type}^*	μ	Stellar Mass $\log(M_*/M_\odot)$	SFR $\log(M_\odot \text{yr}^{-1})$
VLAHFF-J001428.61-302270.98	0.61	p	2.46	10.36	0.73 ± 0.35
VLAHFF-J001426.07-302452.48	2.65	p	2.18	11.12	2.52 ± 1.99
VLAHFF-J001425.35-302550.30	2.90	p	2.26	10.13	2.25 ± 1.89
VLAHFF-J001421.68-302410.26	0.50	s	3.01	10.70	1.05 ± 0.02
VLAHFF-J001419.80-302370.61	2.93	p	4.60	10.00	2.20 ± 1.69
VLAHFF-J001419.51-302248.98	3.55	p	3.14	10.53	2.48 ± 2.02
VLAHFF-J001417.58-302300.58	1.22	p	2.48	09.81	2.22 ± 0.96
VLAHFF-J001413.92-302237.95	2.93	p	9.27	09.74	2.28 ± 1.68
VLAHFF-J001405.71-302217.28	2.12	p	2.06	10.38	2.38 ± 1.94
VLAHFF-J041606.36-240451.20	0.74	s	3.03	10.36	1.11 ± 0.16
VLAHFF-J041606.62-240527.80	1.90	p	2.26	10.03	1.75 ± 0.18
VLAHFF-J041611.67-240419.60	2.20	p	2.26	10.16	1.94 ± 0.15
VLAHFF-J071725.85+374446.20	2.93	p	2.21	10.36	2.16 ± 0.15
VLAHFF-J071730.65+374443.10	1.01	s	2.84	10.43	0.88 ± 0.16
VLAHFF-J071733.14+374543.20	0.91	s	2.11	09.89	1.38 ± 0.14
VLAHFF-J071734.46+374432.20	1.14	s	5.84	09.42	1.56 ± 0.12
VLAHFF-J071735.22+374541.70	1.69	s	3.61	10.87	1.73 ± 0.14
VLAHFF-J071736.66+374506.40	1.13	s	6.45	09.48	1.01 ± 0.15
VLAHFF-J071740.55+374506.40	1.97	p	2.18	10.48	1.83 ± 0.15
VLAHFF-J114932.03+222439.30	1.28	s	2.11	10.19	2.12 ± 0.19
VLAHFF-J114934.46+222438.50	0.75	s	2.16	09.77	0.72 ± 0.13
VLAHFF-J114936.09+222424.40	1.64	p	3.13	10.71	1.67 ± 0.15

Table 3. The sample of 22 moderately/strongly lensed ($\mu \geq 2$) galaxies in the the VLA Frontier Fields survey, including 12 galaxies in the MACSJ0416.1-2403, MACSJ0717.5+3745, and MACSJ1149.5+2223 (Heywood et al. 2021; Jiménez-Andrade et al. 2021) and 9 galaxies in A 2744 reported in this work. * **p** denotes the photometric redshift and **s** denotes spectroscopic redshift.

REFERENCES

- Ananna, T. T., Bogdán, Á., Kovács, O. E., Natarajan, P., & Hickox, R. C. 2024, *ApJL*, 969, L18
- Barro, G., Pérez-González, P. G., Kocevski, D. D., et al. 2024, *ApJ*, 963, 128
- Bean, B., Bhatnagar, S., Castro, S., et al. 2022, *PASP*, 134, 114501
- Bezanson, R., Labbe, I., Whitaker, K. E., et al. 2024, *ApJ*, 974, 92
- Blanton, M. R., Brinkmann, J., Csabai, I., et al. 2003, *AJ*, 125, 2348
- Bonaldi, A., Bonato, M., Galluzzi, V., et al. 2019, *MNRAS*, 482, 2

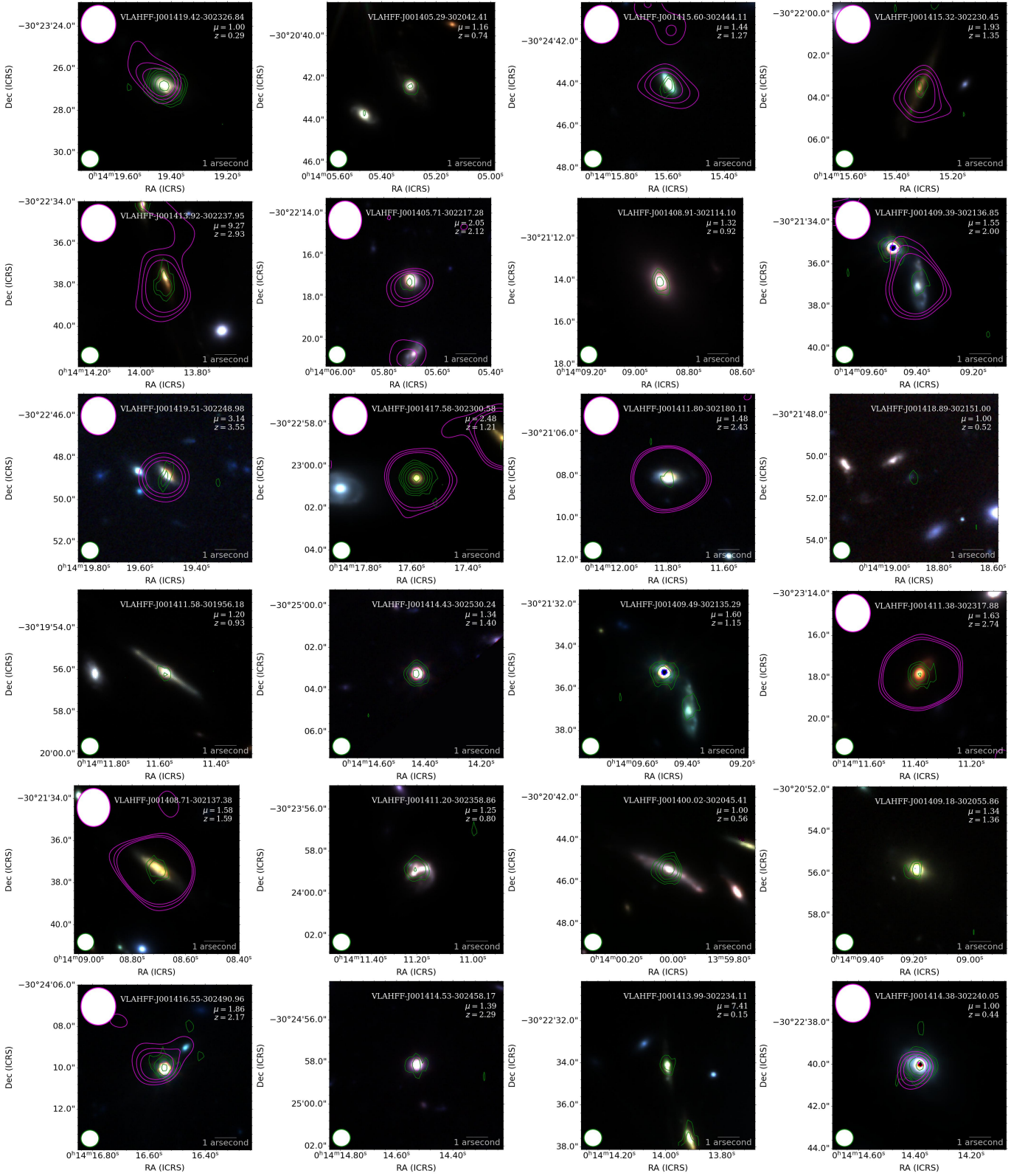


Figure 12. RGB NIRCam (R: F444W, G: F277W, B: F150W) images for the 46 radio sources detected at 6 GHz with a *HST*+*JWST* counterpart, including VLAHFF-J001404.22-301920.31 and VLAHFF-J001415.59-302259.85. The green contours represent the 3 σ , 5 σ , 8 σ , 13 σ , 21 σ , 34 σ and 55 σ significance levels of the VLA images, while the magenta contours represent the 3 σ , 4 σ and 5 σ significance levels of the ALMA 1.2 mm map when available. The green circle in the bottom left represents the VLA synthesized beam (0''.82) and the magenta ellipse at the upper left represents the ALMA synthesized beam (major = 1''.81, minor = 1''.60).

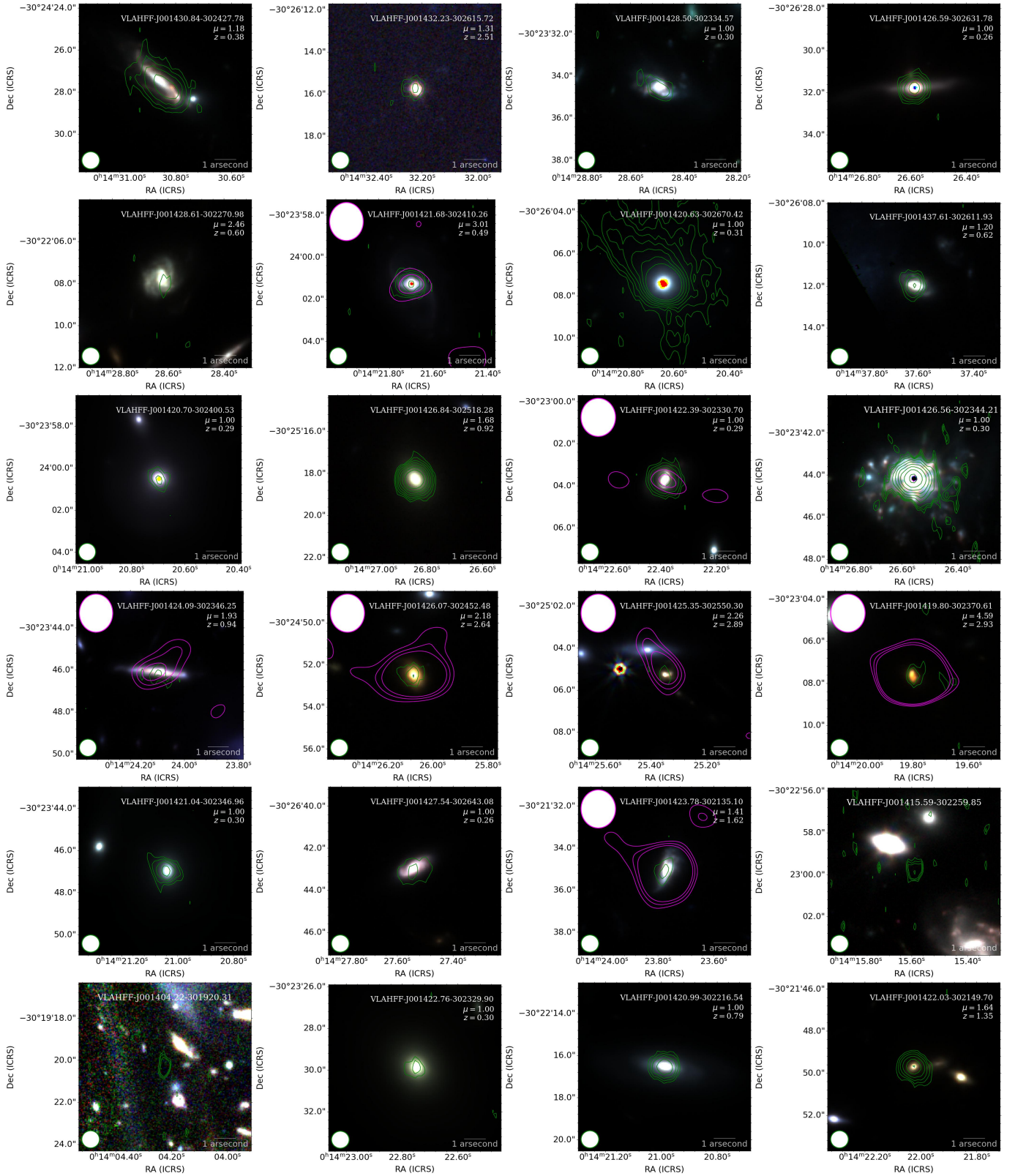


Figure 13. RGB NIRCcam (R: F444W, G: F277W, B: F150W) images for the 46 radio sources detected at 6 GHz with a *HST*+*JWST* counterpart, including VLAHFF-J001404.22-301920.31 and VLAHFF-J001415.59-302259.85 sources. The green contours represent the 3σ , 5σ , 8σ , 13σ , 21σ , 34σ and 55σ significance levels of the VLA images, while the magenta contours represent the 3σ , 4σ and 5σ significance levels of the ALMA 1.2mm map when available. The green circle in the bottom left represents the VLA synthesized beam ($0''.82$) and the magenta ellipse at the upper left represents the ALMA synthesized beam (major = $1''.81$, minor = $1''.60$).

- Bouwens, R., González-López, J., Aravena, M., et al. 2020, *ApJ*, 902, 112
- Calzetti, D. 2001, *PASP*, 113, 1449
- Chapman, S. C., Smail, I., Blain, A., & Ivison, R. 2004, *ApJ*, 614, 671
- Choi, J., Dotter, A., Conroy, C., et al. 2016, *ApJ*, 823, 102
- Condon. 1992, *ARA&A*, 30, 575
- Conroy, C., & Gunn, J. E. 2010, *ApJ*, 712, 833
- Davidson-Pilon, C. 2019, *JOSS*, 4, 1317, doi: [10.21105/joss.01317](https://doi.org/10.21105/joss.01317)
- Delhaize, J., Smolčić, V., Delvecchio, I., et al. 2017, *A&A*, 602, A4
- Dotter, A. 2016, *ApJs*, 222, 8
- Draine, B. T., & Li, A. 2007, *ApJ*, 657, 810
- Evans, I. N., & Civano, F. 2018, *A&G*, 59, 2
- Feigelson, E. D., & Nelson, P. I. 1985, *ApJ*, 293, 192
- Fujimoto, S., Bezanson, R., Labbe, I., et al. 2023, *arXiv preprint arXiv:2309.07834*
- Gludemans, A. J., Duncan, K. J., Eilers, A.-C., et al. 2025, *arXiv preprint arXiv:2501.04912*
- Gómez-Guijarro, C., Elbaz, D., Xiao, M., et al. 2022, *A&A*, 658, A43
- González-López, J., Novak, M., Decarli, R., et al. 2020, *ApJ*, 897, 91
- González-López, Bauer, F. E., Romero-Cañizales, C., et al. 2017, *A&A*, 597, A41, doi: [10.1051/0004-6361/201628806](https://doi.org/10.1051/0004-6361/201628806)
- Greene, J. E., Labbe, I., Goulding, A. D., et al. 2024, *ApJ*, 964, 39
- Harikane, Y., Zhang, Y., Nakajima, K., et al. 2023, *ApJ*, 959, 39
- Helou, G., Soifer, B., & Rowan-Robinson, M. 1985, *ApJ*, 298, L7
- Heywood, I., Murphy, E., Jiménez-Andrade, E., et al. 2021, *ApJ*, 910, 105
- Hopkins, A. M., Miller, C., Nichol, R., et al. 2003, *ApJ*, 599, 971
- Isobe, T., Feigelson, E. D., Akritas, M. G., & Babu, G. J. 1990, *ApJ*, 364, 104
- Jiménez-Andrade, E., Murphy, E., Heywood, I., et al. 2021, *ApJ*, 910, 106
- Johnson, B. D., Leja, J., Conroy, C., & Speagle, J. S. 2021, *ApJs*, 254, 22
- Kamieneski, P. S., Yun, M. S., Harrington, K. C., et al. 2024, *ApJ*, 961, 2
- Kaplan, E. L., & Meier, P. 1958, *JASA*, 53, 457
- Klein, U., Lisenfeld, U., & Verley, S. 2018, *A&A*, 611, A55
- Kocevski, D. D., Onoue, M., Inayoshi, K., et al. 2023, *ApJL*, 954, L4
- Kocevski, D. D., Finkelstein, S. L., Barro, G., et al. 2024, *arXiv preprint arXiv:2404.03576*
- Labbé, I., van Dokkum, P., Nelson, E., et al. 2023, *Nature*, 616, 266
- Labbe, I., Greene, J. E., Bezanson, R., et al. 2024, *ApJ*, 978, 92
- Laigle, C., McCracken, H. J., Ilbert, O., et al. 2016, *ApJs*, 224, 24
- Laporte, Bauer, F. E., Troncoso-Iribarren, P., et al. 2017, *A&A*, 604, A132, doi: [10.1051/0004-6361/201730628](https://doi.org/10.1051/0004-6361/201730628)
- Leslie, S. K., Schinnerer, E., Liu, D., et al. 2020, *ApJ*, 899, 58
- Liu, D., Förster Schreiber, N. M., Harrington, K. C., et al. 2024, *Nat. Astron.*, 8, 1181
- Lotz, J. e., Koekemoer, A., Coe, D., et al. 2017, *ApJ*, 837, 97
- Ma, J., Gonzalez, A. H., Spilker, J., et al. 2015, *ApJ*, 812, 88
- Madau, P. 1995, *ApJ*, 441, 18
- Magnelli, B., Ivison, R., Lutz, D., et al. 2015, *A&A*, 573, A45
- Maiolino, R., Risaliti, G., Signorini, M., et al. 2025, *MNRAS*, 538, 1921
- Mancuso, C., Lapi, A., Prandoni, I., et al. 2017, *ApJ*, 842, 95
- Matthee, J., Naidu, R. P., Brammer, G., et al. 2024, *ApJ*, 963, 129
- Mazzolari, G., Gilli, R., Maiolino, R., et al. 2024, *arXiv preprint arXiv:2412.04224*
- Mohan, N., & Rafferty, D. 2015, *ASCL*, ascl
- Moretti, A., Radovich, M., Poggianti, B. M., et al. 2022, *ApJ*, 925, 4
- Murphy, E., Helou, G., Kenney, J., Armus, L., & Braun, R. 2008, *ApJ*, 678, 828
- Murphy, E. J. 2009, *ApJ*, 706, 482
- Murphy, E. J., Momjian, E., Condon, J. J., et al. 2017, *ApJ*, 839, 35
- Murphy, E. J., Helou, G., Braun, R., et al. 2006, *ApJ*, 651, L111
- Olowin, R. 1988, *PASP*, 100, 1354
- Paul, S., Salunkhe, S., Datta, A., & Intema, H. T. 2019, *MNRAS*, 489, 446
- Pearce, C., Van Weeren, R., Andrade-Santos, F., et al. 2017, *ApJ*, 845, 81
- Perger, K., Fogasy, J., Frey, S., & Gabányi, K. 2025, *A&A*, 693, L2
- Radcliffe, J. F., Barthel, P., Thomson, A., et al. 2021, *A&A*, 649, A27
- Rahaman, M., Raja, R., Datta, A., et al. 2021, *MNRAS*, 505, 480
- Rawle, T., Altieri, B., Egami, E., et al. 2016, *MNRAS*, 459, 1626

- Reuter, C., Vieira, J., Spilker, J., et al. 2020, *ApJ*, 902, 78
- Robitaille, T. P., Tollerud, E. J., Greenfield, P., et al. 2013, *A&A*, 558, A33
- Smail, I., Ellis, R., Fitchett, M., et al. 1991, *MNRAS*, 252, 19
- Smolčić, V., Novak, M., Bondi, M., et al. 2017, *A&A*, 602, A1
- Steinhardt, C. L., Jauzac, M., Acebron, A., et al. 2020, *ApJs*, 247, 64
- Treu, T., Roberts-Borsani, G., Bradac, M., et al. 2022, *ApJ*, 935, 110
- Van Weeren, R., Ogreaan, G., Jones, C., et al. 2016, *ApJ*, 817, 98
- Wang, B., Leja, J., Labbé, I., et al. 2023, *ApJs*, 270, 12
- Wang, B., De Graaff, A., Davies, R. L., et al. 2025, *ApJ*, 984, 121
- Weaver, J. R., Cutler, S. E., Pan, R., et al. 2024, *ApJs*, 270, 7, doi: [10.3847/1538-4365/ad07e0](https://doi.org/10.3847/1538-4365/ad07e0)
- Yue, M., Eilers, A.-C., Ananna, T. T., et al. 2024, *ApJL*, 974, L26
- Zavala, J., Casey, C., Manning, S., et al. 2021, *ApJ*, 909, 165